Chemistry in disks. VI. CN and HCN in protoplanetary disks

E. Chapillon, S. Guilloteau, Anne Dutrey, M. Guélin

A&A 537, A60 (2012)
DOI: 10.1051/0004-6361/201116762

Astronomy & Astrophysics

Chemistry in disks

VI. CN and HCN in protoplanetary disks⋆,⋆⋆,⋆⋆⋆

E. Chapillon[1,2,3,4], S. Guilloteau[2,3], A. Dutrey[2,3], V. Piétu[4], and M. Guélin[4]

[1] MPIfR, Auf dem Hügel 69, 53121 Bonn, Germany
e-mail: echapill@mpifr-bonn.mpg.de
[2] Université de Bordeaux, Observatoire Aquitain des Sciences de l'Univers, 2 rue de l'Observatoire, BP 89, 33271 Floirac, France
[3] CNRS/INSU – UMR 5804, Laboratoire d'Astrophysique de Bordeaux, 2 rue de l'Observatoire, BP 89, 33271 Floirac, France
e-mail: [guilloteau;dutrey]@obs.u-bordeaux1.fr
[4] IRAM, 300 rue de la Piscine, 38406 Saint Martin d'Hères, France
e-mail: [pietu;guelin]@iram.fr

Received 22 February 2011 / Accepted 23 September 2011

ABSTRACT

Context. The chemistry of protoplanetary disks is thought to be dominated by two major processes: photodissociation near the disk surface and depletion on dust grains in the disk midplane, resulting in a layered structure with molecules located in a warm layer above the disk midplane.
Aims. We attempt here to confront this warm molecular layer model prediction with the distribution of two key molecules for dissociation processes: CN and HCN
Methods. Using the IRAM Plateau de Bure interferometer, we obtained high spatial and spectral resolution images of the CN $J = 2$–1 and HCN $J = 1$–0 lines in the disks surrounding the two T Tauri DM Tau and LkCa 15 and the Herbig Ae MWC 480. We have derived disk properties by assuming power-law distributions. The hyperfine structure of the observed transitions allowed us to constrain the line opacities and excitation temperatures. We compare the observational results with predictions from existing chemical models, and used a simple PDR model (without freeze-out of molecules on grains and surface chemistry) to illustrate dependencies on UV field strength, grain size, and gas-to-dust ratio. We also evaluated the impact of Ly α radiation.
Results. The temperature ordering follows the trend found from CO lines, with DM Tau the coldest object and MWC 480 the warmest. Although CN indicates somewhat higher excitation temperatures than HCN, the derived values in the T Tauri disks are very low (8–10 K). They agree with results obtained from C_2H, and contradict thermal and chemical model predictions. These very low temperatures, as well as geometrical constraints, suggest that substantial amounts of CN and HCN remain in the gas phase close to the disk midplane and that this midplane is quite cold. The observed CN/HCN ratio ($\simeq$5−10) is in better agreement with the existence of large grains and possibly also with a substantial contribution of Ly α radiation.

Key words. circumstellar matter – astrochemistry – protoplanetary disks – radio lines: stars

1. Introduction

Studying the physical and chemical structure of protoplanetary disks is a prerequisite for our understanding of planet formation. While much theoretical work has been done on the structure and evolution of these disks (Bergin et al. 2007, and references therein), key parameters, such as gas density and temperature or molecular content and distribution, remain poorly constrained. Since H_2, which represents 80% of the gas mass, cannot be observed with a good spatial resolution, our knowledge of the molecular component relies on low abundance tracers such as CO (Guilloteau & Dutrey 1998). Interferometric maps of disks, revealing their radial and vertical structure. Studies of the rare CO isotopologues, ^{13}CO and C^{18}O, confirm the existence of a vertical temperature gradient (Dartois et al. 2003; Piétu et al. 2007), allowing the first face to face confrontation between model predictions and observations in the outer parts of the disks.

This has led to a global picture of a flared disk consisting of three strata, or layers. The upper layer, close to the disk surface, is directly illuminated by the stellar UV and dominated by photo-dissociation reactions. The lowest layer, near the disk plane, is very cold, so that molecules are expected to be depleted on grains. Between those is the third layer, where the gas is lukewarm and the chemistry dominated by gas-phase reactions. Such a simple picture has already been challenged by new observations that reveal that large amounts of cold CO are still in the gas phase (Dartois et al. 2003; Piétu et al. 2007), contrary to predictions. Vertical mixing was proposed to refurbish CO in the cold zone (Aikawa & Nomura 2006; Aikawa 2007; Semenov et al. 2006; see also Willacy et al. 2006).

In this scheme, molecules are displaced from the upper layers to the cold midplane and have the time to cool down before sticking onto grains; however, the results strongly depend on the grain surface reaction efficiencies and on the disk structure.

⋆ Based on observations carried out with the IRAM Plateau de Bure Interferometer. IRAM is supported by INSU/CNRS (France), MPG (Germany), and IGN (Spain).
⋆⋆ CID is an international collaboration dedicated to the study of Chemistry In proto-planetary Disks.
⋆⋆⋆ Appendices A and B are available in electronic form at http://www.aanda.org

Table 1. Star properties.

Source	Right ascension	Declination	Spec. type	Effective temp. (K)	Stellar lum. ($L_\odot$)	CO paper
MWC 480	04:58:46.264	29:50:36.86	A4	8460	11.5	1, 2
LkCa 15	04:39:17.790	22:21:03.34	K5	4350	0.74	1, 2
DM Tau	04:33:48.733	18:10:09.89	M1	3720	0.25	1, 3

Notes. Columns 2 and 3: J2000 coordinates deduced from the fit of the PdBI 1.3 mm continuum map. Errors on the astrometry are ≤0.05″. Columns 4–6, the spectral type, effective temperature, and the stellar luminosity are those given in Simon et al. (2000). Column 6, CO interferometric papers are: 1 = Piétu et al. (2007), 2 =Simon et al. (2000), 3 = Dartois et al. (2003).

Hersant et al. (2009) have also shown that photodesorption may increase the amount of cold CO in the gas.

A deeper understanding of the disk structure relies on the study of molecules probing different physical and chemical conditions. Apart from CO, only a few molecules show strong enough mm/sub-mm emission to be detected: HCO^+, N_2H^+, HCN, CN, HNC, CCH, CS, and H_2CO (Dutrey et al. 1997; Kastner et al. 1997; Thi et al. 2004; van Zadelhoff et al. 2001). Even fewer can be mapped (Aikawa et al. 2003; Qi et al. 2004; Dutrey et al. 2007; Schreyer et al. 2008). Among those, HCN and CN are particularly interesting because they trace different conditions, and their abundances are closely related: HCN may be photodissociated (e.g., by Ly α radiation from the star) to yield CN (Bergin et al. 2003). One thus expects HCN to trace the UV-shielded lukewarm and cold layers of the disk and CN the uppermost layer.

In this article, we present high angular resolution (3″ to 1.5″) observations of HCN J = 1–0 and CN J = 2–1 emission in three protoplanetary disks. The sources belong to the nearby Taurus-Aurigae star forming region, but have moved outside their parent cloud, so that they can be observed without interference. Table 1 summarizes their stellar properties.

- DM Tau is a classical T Tauri star of mass 0.5 $M_\odot$ surrounded by a disk in Keplerian rotation (Guilloteau & Dutrey 1998; Piétu et al. 2007). Dartois et al. (2003) have shown the existence of a vertical temperature gradient from the high angular resolution observations of several transitions of ^{12}CO, ^{13}CO and C^{18}O. Eight different molecular species have been detected in this source (Dutrey et al. 1997).
- LkCa 15 is a 1 $M_\odot$ T Tauri star surrounded by a disk with a central cavity (Piétu et al. 2006). Piétu et al. (2007) found no evidence of a vertical temperature gradient from their CO multi-isotopologue data. The cavity radius derived from dust emission is ∼45 AU, but some CO gas remains down to 20 AU or so (Piétu et al. 2007).
- Finally, MWC 480 is a Herbig Ae star of 1.8 $M_\odot$ surrounded by a Keplerian disk (Mannings et al. 1997; Simon et al. 2000; Piétu et al. 2007). CO isotopologues indicate a vertical temperature gradient. The disk continuum emission was resolved by Piétu et al. (2006), suggesting even lower temperatures for the dust than from ^{13}CO, but Guilloteau et al. (2011) show that alternative solutions with radially varying dust properties are possible.

Section 2 presents the observations. The method of analysis and the results are shown in Sects. 3 and 4 is dedicated to the chemical modeling. We discuss the implications of our study in Sect. 5 and then we conclude.

2. Observations

All the observations reported here were made with the IRAM Plateau de Bure interferometer (PdBI). The CN J = 2 → 1 observations of DM Tau were performed in Feb., Apr., Sep. and Oct. 1997 with baselines ranging from 15 m to 180 m. The spatial resolution (HPBW) was 1.7 × 1.2″ (PA 122°) for "natural weighting". The HCN J = 1 → 0 data were obtained in Nov. 1999, Jan. 2001, and Jan. 2002 with baselines from 15 to 330 m. The HPBW was 3.7×2.4″ (PA 39°) using natural weighting and 3.0 × 1.8″ at PA 45° for "robust" weighting.

The LkCa15 and MWC 480 data were observed in HCN J = 1 → 0 and CN J = 2 → 1 data in a track-sharing mode to obtain homogeneous calibration for both sources. Baselines ranged from 15 to 330 m, with an emphasis on short baselines: natural weighting yielded an HPBW of 2.2 × 1.3″ (PA 56°) and robust weighting an HPBW of 1.2 × 0.7″ (PA 40°) for CN, and was proportionally larger by a factor 2.5 for HCN.

We used the GILDAS[1] software package (Pety 2005) for the data calibration and deconvolution and as the framework for implementing our minimization method. The resulting velocity-channel maps in the HCN J = 1 → 0 and CN J = 2 → 1 lines are shown in Figs. 2 and 1), and the spectra integrated over the disk are presented in Figs. 4, 3. In MWC 480, the HCN emission is weak, but significant at the 7σ level (see Fig. 5). Channel maps for HCN in MWC 480 line are only presented in Appendix A, which also includes a more complete set of channel maps for all sources, in particular those of the other observed CN hyperfine components. We caution that, although the integrated spectra in Figs. 3–4 were obtained from the Clean images, they underestimate the flux. This is not due to the lack of short spacings, but to the difficulty of deconvolving channel per channel low signal-to-noise data when the synthesized beam has relatively high sidelobes. Furthermore, we stress that this imaging bias has no influence on our derived parameters, since our whole analysis is based on a comparison between model visibilities and actual measurements in the UV plane.

Calibration errors could directly affect the derived temperature and molecular column densities. To minimize the calibration errors, all our flux density scale is based on a comparison with MWC 349, a source with precisely known spectral index of 0.6. In addition, as in Guilloteau et al. (2011), MWC 480 is strong enough in continuum to provide an additional comparison, and the final relative flux scale accuracy is about 5%. Our flux density scale here is identical to the one used by Guilloteau et al. (2011). However, recent recalibration of the MWC 349 flux density at mm wavelengths indicates that this overall scale may be too low by about 10% (Krips et al., in prep.).

The velocity was smoothed to 0.41 km s^{-1} in the cases of MWC 480 and LkCa 15 to produce the velocity-channel maps in Fig. 1 and to 0.206 km s^{-1} in the case of DM Tau, but we used full spectral resolution in the model fitting analysis described below: for CN(2–1), 0.206 km s^{-1} in LkCa 15 and MWC 480, and 0.103 km s^{-1} in DM Tau. For HCN(1–0),

[1] See http://www.iram.fr/IRAMFR/GILDAS for more information about the GILDAS software.

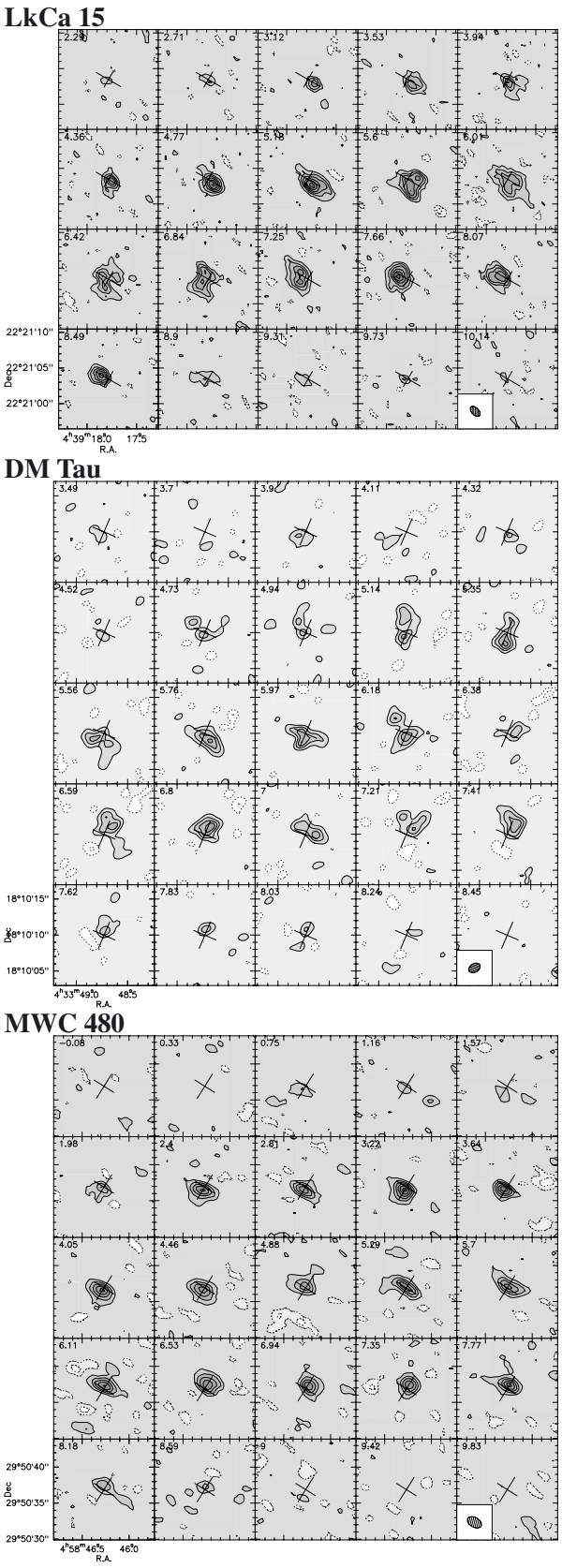

Fig. 1. Channel maps of the CN 2–1 emission for the strongest group of three blended hyperfine components. *Top*: LkCa 15; the spatial resolution is 1.7 × 1.0″ at PA 44°, contour spacing is 60 mJy/beam, or 0.81 K and 2.1σ. *Middle*: DM Tau; the spatial resolution is 1.7 × 1.2″ at PA 120°, contour spacing is 53 mJy/beam, or 0.61 K, 2.0σ. *Bottom*: MWC 480; the spatial resolution is 2.2 × 1.35″ at PA 60°, contour spacing is 55 mJy/beam, or 0.45 K and 2σ.

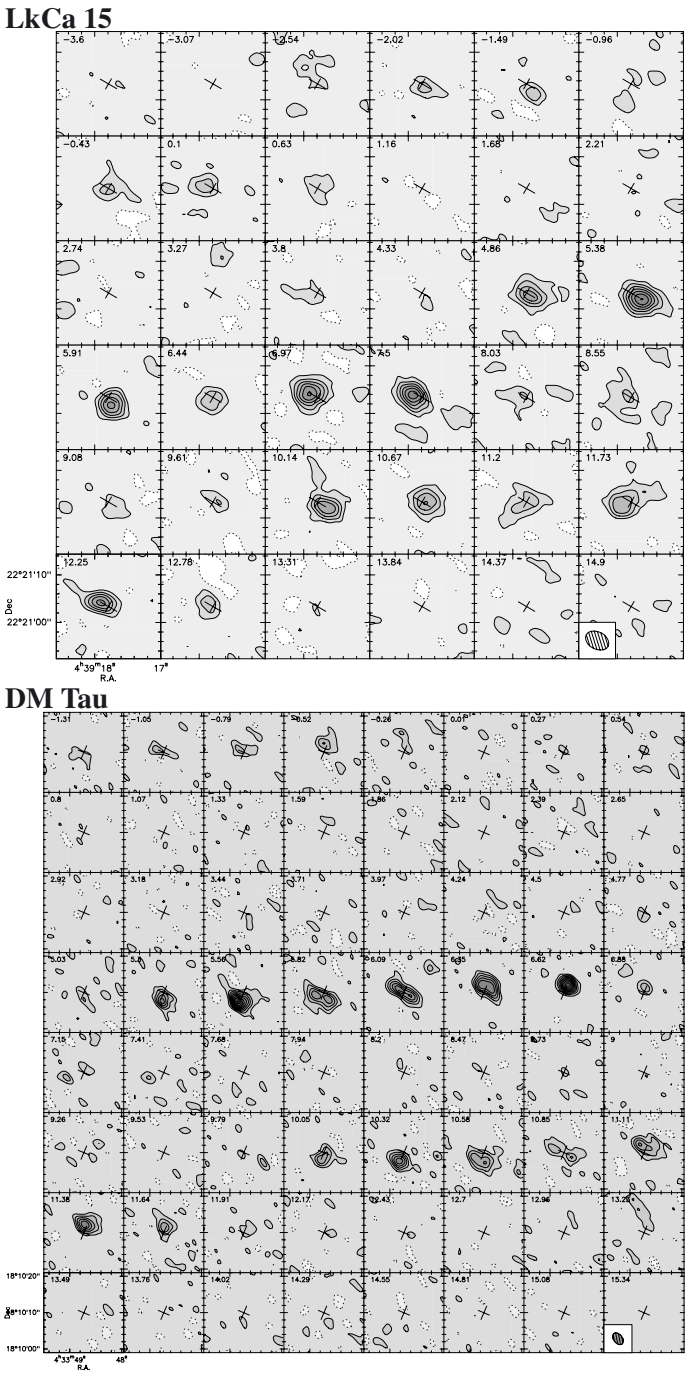

Fig. 2. Channel maps of the HCN 1–0 emission. *Top*: LkCa 15; the spatial resolution is 4.1 × 2.9″ at PA 51°, contour spacing is 16 mJy/beam, or 0.21 K and 2.0σ. *Bottom*: DM Tau; the spatial resolution is 3.7 × 2.4″ at PA 39°, contour spacing is 12 mJy/beam, or 0.21 K, 2.0σ.

spectral resolutions were 0.52 km s^{-1} in LkCa 15, 0.40 km s^{-1} in MWC 480 and 0.26 km s^{-1} in DM Tau. The velocity scale refers to the strongest hyperfine components, i.e. 226.874745 GHz for CN and 88.631848 GHz for HCN.

Prior to this paper, CN and HCN emission had been already detected in several T Tauri and Herbig Ae stars (DM Tau, GG Tau; LkCa 15, HD 163296, MWC 480, and V4046 Sgr), but only with single-dish telescopes, hence at low spatial resolution (Dutrey et al. 1997; Thi et al. 2004; Kastner et al. 2008), except for the most nearby star TW Hya (Qi et al. 2008). A preliminary study of CN(2–1) and HCN(3–2) at ≃2.5″ resolution has been

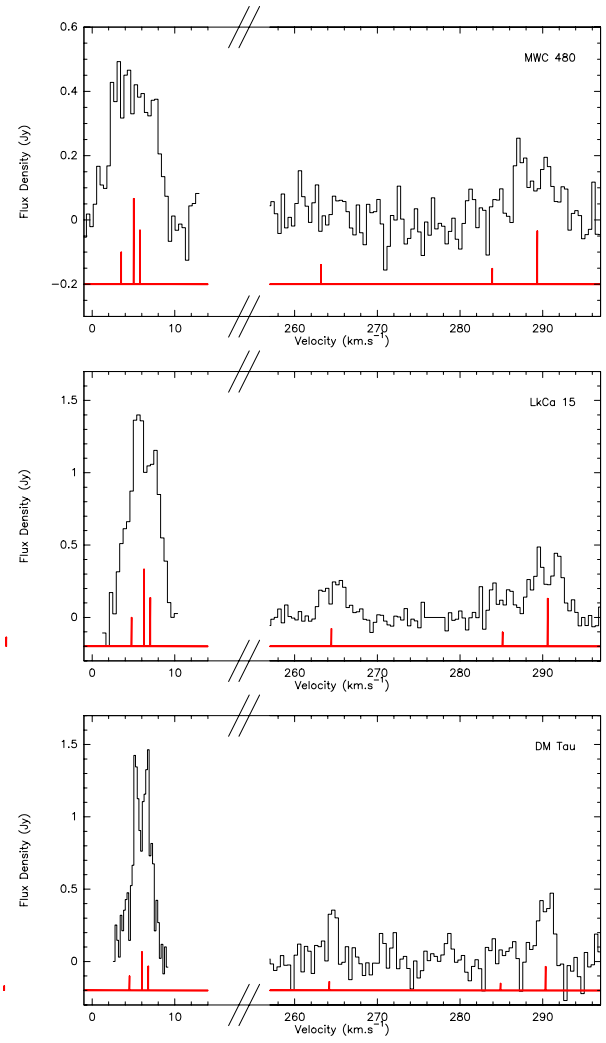

Fig. 3. Integrated spectra for CN 2–1. The relative positions and intensities of the hyperfine components are indicated in red. *Top*: MWC 480; *middle*: LkCa 15; *bottom*: DM Tau

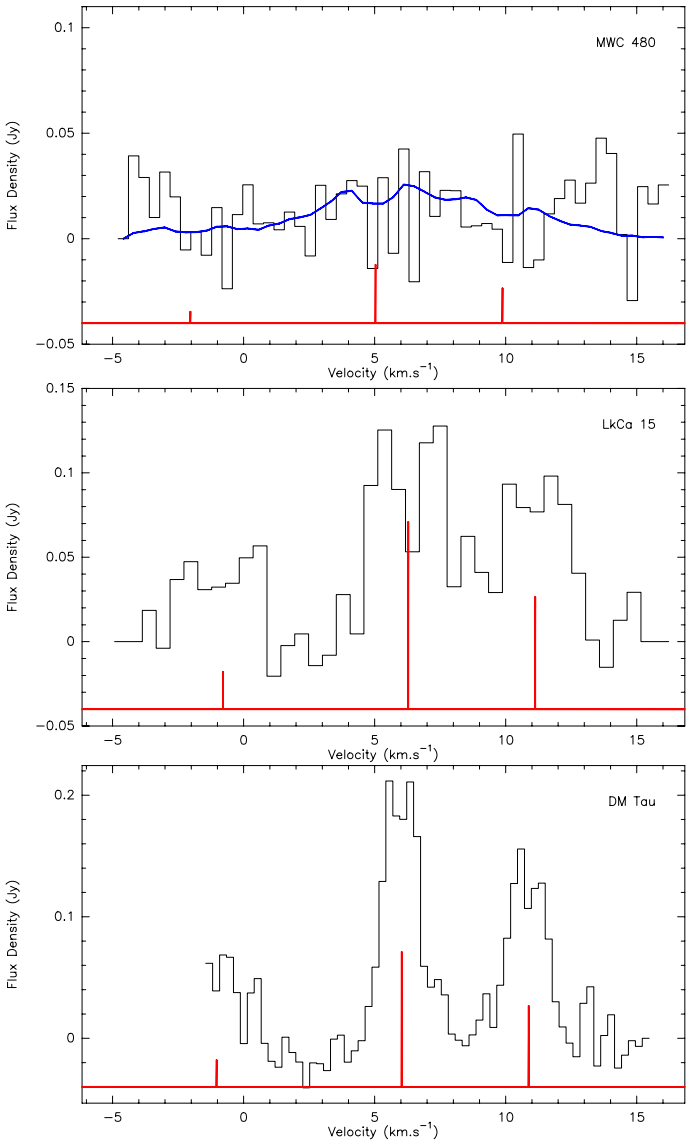

Fig. 4. Integrated spectra for HCN 1–0. The relative positions and intensities of the hyperfine components are indicated in red. *Top*: MWC 480, with the best-fit model (see Table 4) superimposed to illustrate the weak detection; *middle*: LkCa 15; *bottom*: DM Tau

Table 2. Integrated flux of CN and HCN lines.

	S_ν (Jy km s^{-1})		
	DM Tau	LkCa 15	MWC 480
HCN J = 1–0	0.4[a]		
CN J = 1–0	1.4[a]	–	–
CN J = 2–1	8.7[a]/4.7[c]	6.8[c]	3.3[c]
HCN J = 3–2	2.9[c]	5.5[c]	2.3[c]
CN J = 3–2	–	12[b]	5.3[b]
HCN J = 4–3	–	4.6[b]	<1.3[b]

Notes. Integrated line intensities from [(a)] IRAM 30 m observation (Dutrey et al. 1997) and [(b)] JCMT observation (Thi et al. 2004). The conversion factor between Jansky to Kelvin (main beam temperature) for the JCMT (beam ∼13.5″) at 345 GHz is 18.2 Jy/K. [(c)] SMA data from Öberg et al. (2010).

published recently by Öberg et al. (2010). The observations relevant to our sources are summarized in Table 2.

3. Method of analysis and results

Although the velocity-channel maps of Figs. 1 and 2 were produced from the dirty images via clean-based deconvolution, the disk properties were derived directly from the observed visibilities through a model fitting. For this, we used the disk model and hypothesis described in Piétu et al. (2007). We assume circular symmetry. The surface density of molecules follows a power-law of exponent p in radius r; and perpendicular to the plane of the disk, the density of molecules follows a Gaussian of half-width at $1/e$ intensity (scale height) $h(r)$. We further assume the population of each molecular species can be represented by a rotation temperature T, which only depends on r and follows a power-law of exponent q. The disk is thus described by

$$T(r) = T_0(r/R_0)^{-q} \quad (1)$$

$$\Sigma(r) = \Sigma_0(r/R_0)^{-p} \quad (2)$$

$$h(r) = H_0(r/R_0)^{-h}, \quad \text{with } h = -1.25, \quad (3)$$

plus a constant turbulent width δV and an inner and an outer radius. If the molecule is at LTE, $T(r)$ is equal to the kinetic temperature.

3.1. Minimization technique

The minimization technique used to derive the disk parameters was described by Piétu et al. (2007). The continuum emission was subtracted in the UV plane prior to the analysis, rather than being fitted simultaneously. As explained by Piétu et al. (2007), temperature and surface densities can be derived by the minimization procedure from a single transition, even without hyperfine (hf) structure, under the assumption of power-law distributions, provided the spatial resolution is high enough to partially resolve the optically thick core. This is because the shape of the radial dependence of the brightness changes when the line becomes optically thick, from $T_b(r) = T(r)$ in the optically thick region to a function of surface density and temperature in the optically thin domain (e.g. $T_b(r) \propto \Sigma(r)/T(r)$ at high temperatures). Lines with hf components yield additional information that may even allow us to test the power-law hypothesis.

Handling of the hf components in the modeling requires additional care. Under our assumption of common excitation temperature, the apparent hf intensity ratios should only depend on the line opacities. However, when comparing model and observations, limited spectral resolution and discrete velocity sampling may introduce a bias. First, the spectral backend delivers the flux integrated over a channel width and not just sampled at the channel frequency. Second, the separation between the hf components is not an integer multiple of the velocity sampling. In the case of HCN, the intrinsic line widths are comparable to the channel resolution; then, the difference between sampled and integrated values, combined with different sampling for each hf component, may change the predicted hf intensity ratios, which in turn leads to incorrect opacities and to erroneous temperatures and surface densities. We ensured that no such bias is introduced by comparing the results obtained directly from the disk model by using the same sampling in frequency as in the real data to those derived with a much higher sampling, followed by a smoothing that simulates the channel widths and center frequencies. We found almost no differences between the two sets of results, except for a very small (0.02 km s^{-1}) increase in the line width. The hf line intensity ratios were almost identical. In the case of CN, the intrinsic spectral resolution, 0.05 km s^{-1}, is low compared to the line widths.

In the minimization procedure, all HCN hf components were fitted together assuming a common excitation temperature. For CN, the hf components were used in the analysis in two ways: all together and the intrinsically strong and weak components separately. The three sets of results were then compared.

3.2. Analysis of CN and HCN lines

In a first step of the analysis, all geometric parameters of the disk were left free. The derived parameter values were in complete agreement with those derived by Piétu et al. (2007) from CO, but had a lower accuracy as the lines are weaker. Accordingly, we fixed the inclination and position angle of the disk, as well as the stellar mass and gas scale height using Piétu et al. (2007) values (see Table 3). For LkCa 15, we fixed the internal radius R_{int} to 38 AU, a compromise between the CO and dust inner radii from Piétu et al. (2006, 2007). In a second step, only Σ_0 and p (the value and exponent of the surface density law), R_{out}, the outer radius, T_0 and q (the value and exponent of the temperature law), and δV, the local line width of each molecule, were fitted.

In addition, since many chemical models predict that all molecules should be frozen onto dust grains close to the disk midplane, we therefore tested models in which the molecules are present only above the disk plane. We tested two different parameterizations. Parametrization (1) is a simple geometric constraint, in which molecules only exist above $z(r) = \alpha_d h(r)$, with α_d (the "depletion scale height") a free parameter; i.e.,

$$X_m(r, z) = 0 \text{ for } z < \alpha_d h(r) \quad (4)$$

where X_m is the molecular abundance. However, the chemical model of Aikawa & Nomura (2006) suggests that, in any given disk, molecular abundances depend essentially on the (molecular hydrogen) column density between the disk surface and the location in the disk. Thus, at large radii, molecules get closer to the disk plane than at smaller radii. As our measurements are most sensitive to the 150–400 AU region, assuming a constant α_d as above may be inappropriate. We thus also considered a second option, where molecules are only present in the upper disk down a constant depth in (molecular hydrogen) column density, Σ_d, the "depletion column density"; i.e.,

$$X_m(r, z) = 0 \text{ for } \int_z^\infty n(r, \zeta)\mathrm{d}\zeta > \Sigma_d, \quad (5)$$

which in the isothermal approximation yields

$$X_m(r, z) = 0 \text{ for } \frac{\Sigma(r)}{2} \operatorname{erfc}\left(\frac{z}{h(r)}\right) > \Sigma_d, \quad (6)$$

where erfc is the complementary error function. This second option is likely to be more realistic, because it avoids placing molecules far off the plane at large distances. Note that $\alpha_d = 0$ corresponds to large Σ_d (equal to the H_2 column density).

Table 3. Modeling: fixed parameters.

Parameters	DM Tau	LkCa 15	MWC 480
PA (°)	65	150	58
i (°)	–35	52	37
V_{lsr} (km s^{-1})	6.00	6.28	5.02
V_{100} (km s^{-1})	2.15	2.90	4.05
R_{int} (AU)	1	38	1

Notes. The parameters are taken from Piétu et al. (2006, 2007).

3.3. Results

The disks of the two T Tauri stars, DM Tau and LkCa 15, display very similar properties (see Table 4). Both show very low CN and HCN rotation temperatures, and their strongest hf line components have moderate optical depth around 100 to 300 AU. The fit to the weakest, optically thinner CN hf components yields a nearly flat surface density distribution, and the fit to the stronger hf components a much steeper one. As a consequence of our single power-law hypothesis, the temperature distributions follow the opposite trend; i.e., the temperature decreases faster for increasing r for the optically thin lines. Such behavior may indicate that the single power-law is not an appropriate representation of the CN distribution and that the density falls faster in the outer parts of the disk (which are hardly detected in the weaker components) than in the inner parts. A close examination of the shape of the χ^2 surface, as a function of the exponents p and q, indeed reveals a broad, curved, and relatively shallow global minimum for the strong hf components, with two local minima that correspond to the two (flat and steep) solutions just described.

Table 4. Results of analysis.

Source	Molecule	Σ (10^{12} cm^{-2})	p	R_{out} (AU)	δV (km s^{-1})	T_k (K)	q	α_d
MWC 480	HCN 1–0	1.1 ± 0.4	2.4 ± 0.4	[550]	0.3 ± 0.2	[30]	[0]	0.0 ± 0.7
	CN 2–1 (strong)	11 ± 1	2.1 ± 0.1	540 ± 40	0.25 ± 0.04	33 ± 6	[0]	0.0 ± 0.3
	CN 2–1 (weak)	11 ± 1.2	2.1 ± 0.15	550 ± 70	0.26 ± 0.07	33 ± 6	[0]	–
	CN 2–1 (all)	10.4 ± 0.9	2.1 ± 0.1	545 ± 35	0.25 ± 0.04	30 ± 4	[0]	–
LkCa 15	HCN 1–0	10.6 ± 1.5	1.1 ± 0.2	600 ± 40	0.20 ± 0.03	7.0 ± 0.6	0.55 ± 0.25	0.0 ± 0.8
	CN 2–1 (strong)	38 ± 4	2.3 ± 0.2	570 ± 20	0.18 ± 0.02	10.8 ± 0.7	0.20 ± 0.07	0.15 ± 0.17
	CN 2–1 (weak)	115 ± 18	0.2 ± 0.2	690 ± 20	0.26 ± 0.03	6.6 ± 0.3	0.80 ± 0.07	–
	CN 2–1 (all)	58 ± 5	0.8 ± 0.1	630 ± 35	0.18 ± 0.01	8.8 ± 0.3	0.95 ± 0.05	–
DM Tau	HCN 1–0	6.5 ± 0.9	1.0 ± 0.3	660 ± 20	0.18 ± 0.01	6.0 ± 0.4	0.00 ± 0.12	0.0 ± 0.5
	CN 2–1 (strong)	26 ± 4	2.1 ± 0.15	650 ± 20	0.16 ± 0.01	8.6 ± 0.5	0.05 ± 0.05	0.0 ± 0.3
	CN 2–1 (weak)	46 ± 9	0.7 ± 0.15	550 ± 25	0.20 ± 0.01	6.5 ± 0.5	0.50 ± 0.08	0.0 ± 0.3
	CN 2–1 (all)	35 ± 9	0.6 ± 0.06	620 ± 15	0.17 ± 0.01	7.5 ± 0.3	0.60 ± 0.05	0.0 ± 0.3

Notes. Column density $\Sigma(r) = \Sigma \times (r/R_0)^{-p}$, external radius R_{out}, local line width δV, temperature $T(r) = T \times (r/r_0)^{-q}$ and depletion scale height α_d (see text). All values are referred to $r_0 = 300$ AU. Square brackets indicate fixed parameters. The error bars are 1 σ uncertainties, and do not include uncertainties from calibration.

We attempted fitting all components with a model including two power-laws (crossing at some radius R_x), but did not find any noticeably better results; in most cases, the fit converged towards one of the two single power-laws identified already. The rotation temperatures derived when varying R_x remained within the range of temperatures allowed by the single power-law fits as listed in Table 4.

Within the hypothesis where molecules are only in a surface layer, the depletion parameter α_d can be constrained from the observations (see Semenov et al. 2008), because the distribution of molecules is reasonably well described by two thin disks with slightly different inclinations, so that their projected kinematic patterns differ. We find $\alpha_d \simeq 0$ ($\alpha_d = 0 \pm 0.3$ for the more sensitive CN measurements – see Table 4), indicating that the detected molecules are most likely concentrated close to the disk plane.

For the second approach, we must provide the underlying H_2 density profile. We assumed two different disk models for the H_2 density based on the analysis of the millimeter continuum emission performed by Guilloteau et al. (2011). The first is a power-law distribution; however, although the millimeter continuum emission indicates outer radii of 200–300 AU, we extrapolate the H_2 surface density up to 800 AU, which leads to a model with unlikely high densities at large radii. The second one uses the exponentially tapered solution of self-similar viscous evolution. Both solutions have similar surface densities near 100 AU, but differ in the outer parts, i.e. beyond 200–250 AU. The H_2 surface density is about 4×10^{23} cm^{-2} near 100 AU. It decreases as $r^{-0.8}$ for the power-law model, while the exponential taper leads to much steeper decline beyond 300 AU. For CN, the derived "depletion column density", Σ_d, depends somewhat on the disk model. For DM Tau, we find $\Sigma_d = 3^{+1}_{-0.7} \times 10^{22}$ cm^{-2} for the power-law and $\Sigma_d = 8 \pm 1 \times 10^{22}$ cm^{-2} for the viscous model. In the former case, the error is highly asymmetric: the 3 and 4σ lower limits are $\Sigma_d = 2$ and 1×10^{21} cm^{-2} respectively.

For the Herbig star (MWC 480), the sensitivity of our observations is not good enough to derive both T and q. Nevertheless, if assuming a slope $q = 0$, a value of $T = 30$ K is fitted for the CN emission. That is in accordance with the expected kinetic temperature of the molecular layer in the theoretical models. Using $q = 0.4$ instead results in a temperature $T(300\ \mathrm{AU}) = 14$ K, but affects neither the derived surface density (by less than 5%) nor the exponent p (by less than 0.1). This is because in the 10–30 K temperature range, the CN $J = 2$–1 line brightness weakly depends on the temperature (see Dartois et al. 2003, their Fig. 4, given for CO but also applicable to CN). For HCN, which has low signal-to-noise ratio, we assumed the same temperature ($q = 0$, $T = 30$ K) and outer radius as derived from CN. Although arbitrary, this choice is justified by the results found for DM Tau and LkCa 15, where CN and HCN display similar rotation temperatures and outer radii.

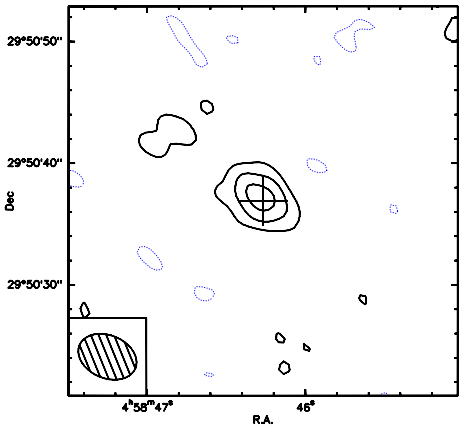

Fig. 5. Signal-to-noise image for the HCN $J = 1$–0 integrated emission in MWC 480 (after removal of the continuum emission), with a velocity weighting profile equal to the best-fit integrated model profile shown in Fig. 4. Contours are in steps of 2σ.

The detection of HCN in MWC 480 is not easily illustrated, because the line intensity is spread over the three hyperfine components of the $J = 1$–0 line. The best-fit profile is shown in Fig. 4. Figure 5 shows a signal-to-noise image obtained using the optimal filtering as described by Dutrey et al. (2007), i.e. weighting each channel by its modeled integrated intensity prior to averaging in velocity. There, the peak signal-to-noise is around seven, and clearly points toward the MWC 480 star, thereby unequivocally showing the reality of the line emission from HCN.

All temperatures may be increased by 10% to account for the calibration issues mentioned in Sect. 2. Although not as linear as for the temperature, an effect of similar magnitude is expected on the molecular surface densities. However, the calibration uncertainties do not affect q, p, R_{out}, α_d or Σ_d, which only depend the shape of the brightness distribution.

4. Chemistry modeling

Generic chemical models of circumstellar disks have been published by Aikawa & Herbst (1999), Willacy & Langer (2000), Aikawa et al. (2002), van Zadelhoff et al. (2003), Aikawa & Nomura (2006), Willacy et al. (2006) and Fogel et al. (2011). Each of these works introduces a different degree of complexity. Aikawa & Herbst (1999) consider gas phase chemistry, along with sticking and desorption, and assume a vertically isothermal disk model following the "minimum mass solar nebula" extended to 800 AU. The study from Willacy & Langer (2000) use the thermal structure derived from the Chiang & Goldreich (1997) two-layer approximation, as well as enhanced photodesorption yields following Westley et al. (1995). Aikawa et al. (2002) use a D'Alessio disk model including vertical temperature gradients and self-consistently variable flaring, although dust and gas are assumed to be fully thermally coupled. All three models use a 1+1D approximation for radiative transfer, in which the stellar UV is attenuated along the line of sight to the star, while the ISRF impacts isotropically on the disk surface. van Zadelhoff et al. (2003) improved the UV treatment by using a 2-D radiative transfer code to solve for the UV field inside the disk, as did Fogel et al. (2011). Shielding by H_2 is treated in an approximate way, however. Aikawa & Nomura (2006) expanded the models further by considering the effect of grain growth, and Fogel et al. (2011) investigated the effects of dust settling following the prescription by D'Alessio et al. (2006). With the exception of Fogel et al. (2011) and Willacy et al. (2006), none of these models include any grain-surface chemistry, which may be important in such environments. However, all of them predict that CN is constrained to a warm molecular layer, sometimes well above the disk plane and that molecules are depleted in the disk plane. The column densities of CN and HCN do not vary much with radius. For a more direct comparison with our results, we fitted the column densities predicted by the chemical models by power-laws as function of radius; i.e., we derived Σ_0 and p.

The model from Willacy et al. (2006) is somewhat different, as it also includes turbulent diffusion, so we discuss it later. A more elaborate set of grain surface chemistry has been included by Walsh et al. (2010), who also find a similar layered structure.

Existing chemical models are not necessarily tailored to the sources we have observed. To better understand the impact of some unknown properties of the observed disks (e.g. UV flux, mass, dust size), we performed new chemical network calculations. The objective of these calculations is not to find an appropriate model for each of the observed disks, but to illustrate common properties of disk chemical models, and pinpoint the dependency between the disk parameters and the predicted molecular column densities. We focus here on CN, which is predicted to be formed mainly in the "warm" photodissociation layer, where chemical reactions are fast. This allows us to use a time-independent chemical model, rather than a more computer-intensive time-dependent one, as would be needed for molecules formed deeper in the disk.

4.1. PDR code

We use the PDR code from the Meudon group (Le Bourlot et al. 1993; Le Petit et al. 2006) modified to account for a nonuniform grain size distribution (see Chapillon et al. 2008). The chemical model assumes a one-dimensional stationary plane-parallel slab of gas and dust illuminated by an ultraviolet (UV) radiation field. The radiative transfer in the UV takes self and mutual shielding of H, H_2, and CO lines into account, as well as absorption and diffusion of the continuum radiation by dust grains in a 1D geometry. Molecular abundances and, optionally, thermal balance of the dust grains and the gas are calculated iteratively at each point in the cloud. The chemical network is similar to that of Goicoechea et al. (2006). The chemical model does not consider the freeze-out of atoms and molecules onto grains and surface chemistry reactions, with the notable exception of those leading to the formation of H_2.

The assumed grain size distribution is a standard power-law $n(a) \propto a^{-\gamma}$, where a_+ and a_- are the maximum and minimum cutoff radii, respectively. The introduction of a range of grain sizes affects the UV extinction curve, the rate of H_2 formation, and the thermal balance of the gas. The resulting extinction curve is calculated using the Mie theory for homogeneous isotropic spherical particles. The composition of the dust is 50% silicate and 50% graphite. We assume $\gamma = -3.5$ (the value observed in nearby interstellar clouds) and $a_- = 3$ nm in all calculations. This minimum grain radius $a_- = 3$ nm is chosen small enough to properly account for the photoelectric heating process, the UV extinction, and the formation of H_2.

Keeping the dust mass constant, we have simulated grain growth by varying the maximum radius a_+(0.3 μm–0.1 mm) while, keeping the exponent γ constant for the sake of simplicity. The amount of small grains is therefore reduced to the benefit of large grains, modifying the extinction curve accordingly. With $\gamma = -3.5$ kept constant, the UV opacity scales as $1/\sqrt{a_+}$ for $a_+ > 10\,\mu$m (see Chapillon et al. 2008).

The chemistry code is one-dimensional and calculates the temperature, radiation field, and molecular abundances in the direction perpendicular to the surface, which we assume here is perpendicular to the disk plane. The justification for such an approach is that small dust grains in the upper disk atmosphere scatter (half of) the incident UV flux towards the disk. We mimic the second dimension by resuming the calculation at different disk radii (12 to 15 different radii from 50 AU to the external radius $R_{\rm out}$), the output being a 1+1D model (see Chapillon et al. 2008, for more details).

4.2. Set of PDR models

We have explored a range of parameters to understand the effects of UV field intensity, grain size, and cosmic ray ionization rate. Three basic disk models (with different density and temperature structure) are used to represent the three sources DM Tau, LkCa 15, and MCW 480. The input disk structure is similar to those of D'Alessio et al. (1999). The density and (dust) temperature distributions were computed self-consistently from the disk masses and stellar properties of each source by Wiebe & Semenov (priv. comm.) assuming uniform grain size of 0.1 μm. The disk models display a vertical temperature gradient, the temperature increasing with height (e.g. Chiang & Goldreich 1997). Except when otherwise noted, we assumed the gas temperature to be equal to the dust temperature. The elemental abundances used are given in Table 5.

For each disk, we varied several parameters.

Grain distribution: we simulated grain growth by varying the maximum radius a_+: in the "big grains" case $a_+ = 0.1$ mm, in the "small grains" case $a_+ = 0.3\,\mu$m.

The incident UV field: the disk surface is illuminated by the sum of the interstellar UV field (ISRF, due mainly to the surrounding massive stars) and the stellar UV field coming from the central star. T Tauri spectra present strong UV excess due to shock accretion of material onto the star. This UV field is assumed to follow the shape of an ISRF Draine field with an

Table 5. Elemental abundances with respect to total hydrogen.

Element	Abundance
C	1.38×10^{-4}
O	3.02×10^{-4}
N	7.954×10^{-5}
Mg	1.0×10^{-8}
S	2.0×10^{-6}
Si	1.73×10^{-8}
Fe	1.7×10^{-9}

intensity scaling factor χ at $r = 100$ AU. This UV field decreases with increasing radius as $1/r^2$. According to Herbig & Goodrich (1986), $\chi = 10^4$ is appropriate, but Bergin et al. (2003) find a much lower value, $\chi = 500$. Using the measurements from Bergin et al. (2003), Henning et al. (2010) derived UV fluxes for DM Tau ($\chi = 300$), LkCa 15 ($\chi = 1850$) and MWC 480 ($\chi = 5000$) (see their Table 1). Accordingly, we explored the range $\chi = 10^3$–10^4 and also ran also some additional models with $\chi = 10^2$ to see the impact of the stellar UV field intensity on the CN/HCN chemistry.

In addition, a couple of models were run for DM Tau with the photodissociation rates calculated without UV excess, but for a black body at 4000 K using rates from van Dishoeck et al. (2006). Results are only presented in Fig. 8.

The cosmic ray ionization rate (CR): we performed calculations with the standard value of 10^{-17} s^{-1} and an increased rate of 5×10^{-17} s^{-1}.

Physical structure: in addition to the values intrinsic to the basic disk models, we varied the density (by a factor of 3) and the temperature (by ±30%) around those values. In the latter case, the scale height was not recomputed, but kept equal to that of the basic model.

Thermal balance: the thermal balance was only computed at $R = 300$ AU in a few models (those presented in Fig. 10), the incident UV field being the main energy source. The dust temperature was derived following Burton et al. (1990) and used to compute the energy exchange between the gas and the grains, as described in Burke & Hollenbach (1983). The gas temperature is then calculated, taking heating and cooling processes into account (see Le Petit et al. 2006, for more details). Again, the scale height is that of the basic model and is not modified consistently.

Ly α line: Bergin et al. (2003) point out the possible importance of the Ly α line on the chemistry. Essentially, HCN can be photodissociated by Ly α radiation, while CN cannot. As the Ly α line can be very strong in the spectra of T Tauri (carrying up to a few 10% of the UV energy), this affects the photodissociation rate, hence the CN/HCN chemistry. To test the influence of Ly α radiation, we implemented its impact on the chemistry following van Dishoeck et al. (2006), and ran a few models in which the Ly α line represents 1/3rd of the total UV luminosity.

Unless otherwise specified, the model parameter values are as follows: $a_+ = 0.3$ μm (i.e. small grains), ISRF UV field with $\chi = 10^3$ and no Ly α included, CR = 10^{-17} s^{-1}, nominal density and temperature, and no thermal balance calculated.

4.3. PDR modeling results

The column densities predicted by the chemical model are fitted by power-laws as functions of radius, and are thus characterized by the values of the Σ_{300} and p, as for the observations. Power-laws offer fairly good approximations to the resulting distribution of column densities.

The calculated Σ_{300} and p as a function of the various input parameters are illustrated for DM Tau in Fig. 6 for CN and Fig. 7 for HCN. The impact of the model parameters is shown in a more compact form for all sources in Fig. B.1. A comparison with other chemical models, fitted in the same way, is displayed in Fig. 8, together with the observed values. The main results are:

- The calculated column densities (at 300 AU) Σ_{300} match the observed values reasonably well (within a factor of a few for the best set of parameters), but the radial dependence (see parameter p) is weaker in the models (p(mod) < p(obs)).
- The most influential parameters are the UV flux and the grain sizes. These two parameters control the photodissociation process.
- As a consequence a high CN/HCN ratio is observed for large grains.
- A modification of the CR influences the HCN/CN chemistry only in the case of small grains, i.e. when UV penetration is efficiently blocked.
- Despite the lack of molecule freeze out and grain chemistry, our PDR code results for CN and HCN are in broad agreement (flat radial distribution and similar value of column densities within a factor of a few) with published results of models that take these processes into account: see Aikawa & Herbst (1999, Figs. 7–9), Aikawa et al. (2002, Fig. 3), van Zadelhoff et al. (2003, Figs. 5 and 8), Aikawa & Nomura (2006, Fig. 9). This suggests that the freeze-out of molecules onto grains, as implemented in these works, does not significantly affect HCN, especially not CN, which remain dominated by photochemistry in these models; however, Walsh et al. (2010) find the grain surface chemistry decreases the HCN column density, but only mildly affect CN.

As in the other chemical studies, the CN molecule is located within a narrow layer close to the surface ($A_V \sim 0.1$ corresponding to $z \sim 200$ AU ($n \sim 5 \times 10^5$ cm^{-3}) in the small grain case and $z \sim 50$ AU ($n \sim 7 \times 10^6$ cm^{-3}) in the big grain case), whereas HCN is buried more deeply inside the disk. The vertical distribution of molecules at $r = 300$ AU are presented in Fig. B.2 for small and big grains and two different values of the incident UV field. As we do not include sticking onto grains, HCN remains fairly abundant in the midplane in contrast to models including sticking onto grains where HCN is not present under $z/r \sim 0.1$ (e.g., Aikawa & Nomura 2006).

Relative abundances can be a misleading indicator of the location of the bulk of molecules, because of the strong vertical density gradient. To better indicate where molecules appear, we trace in Fig. 9 the cumulative column density from the disk midplane to the surface as a function of the gas density. The latter can be converted into height above the disk midplane using the vertical distribution. The temperature (which, in this model, applies equally to gas and dust) is also displayed. Figure 9 shows the temperatures and densities at which the bulk of the column density is built up, allowing prediction of what is the average line excitation temperature. For essentially all models the CN column density is mostly built up in a region where the kinetic temperature is ≥30 K and at a density $n \geq 10^6$ cm^{-3}, the only exception being the small grains, low UV ($\chi = 10^2$) case, where only half of the CN column density show these conditions.

Similar results are obtained in models for which the gas and dust thermal balance is computed. The vertical distributions of CN and HCN abundances are not significantly affected, although the gas temperature is in general somewhat higher in this case

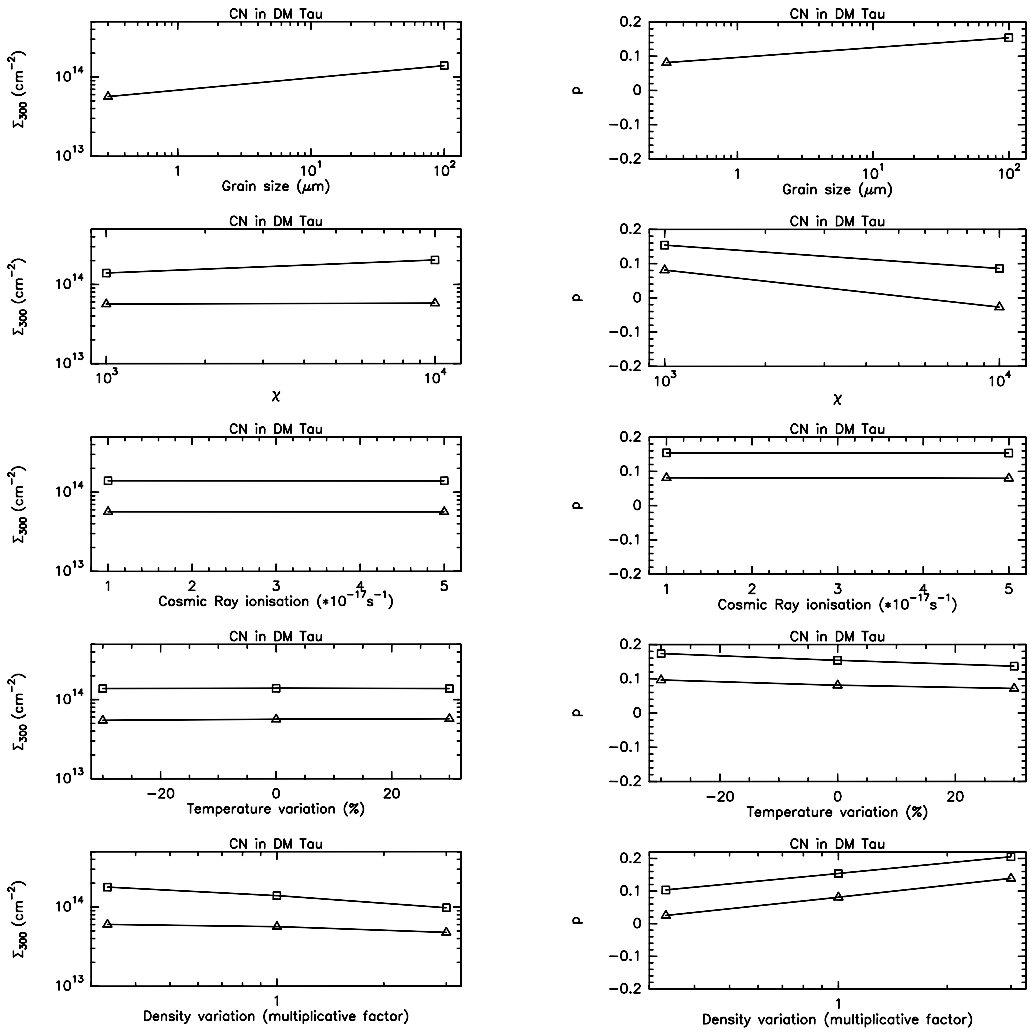

Fig. 6. Variations in the radial distribution of CN (Σ_{300} and p parameters) according to the maximum grain size a_+, the UV field intensity (χ factor), the rate of cosmic ray ionization, and modification of the physical structure. The "standard" values are $\chi = 10^3$, CR = 10^{-17} s^{-1}, and nominal temperature and density structure. Squares: big grains ($a_+ = 0.1$ mm); triangles: small grains ($a_+ = 0.3\,\mu$m).

(Fig. 10). The chemistry is not significantly affected because most reactions depend weakly on the temperature in this temperature range.

5. Discussion

The results from our power-law model fitting of the observations of the T Tauri stars DM Tau and LkCa 15 appear to contradict the chemical model predictions on several aspects.

1. While ^{12}CO indicates temperatures in the range 20 to 30 K at 100 AU for the upper layers (Piétu et al. 2007), the derived CN and HCN rotation temperatures, which mainly apply to radii 100–300 AU, where our observations are the most sensitive, are very low (8 to 12 K, including calibration errors).
2. In addition, the constraint on $\alpha_d \simeq 0$ (equivalent to large Σ_d) suggests that CN molecules appear closer to the disk than expected. This is coherent with a low temperature, but apparently contradicting the location of the predicted molecular layers.
3. Most models predict slopes p that are much lower than observed, the main exception being the results of Aikawa & Herbst (1999) for CN.

For the Herbig star (MWC 480), the temperature may be adequate, but the slope problem remains. This leads to several open questions:

1. Do we understand the basic physical structure (density, temperature) of protoplanetary disks correctly?
2. How a misleading structure can affect the line formation?
3. Do we understand the chemistry, in particular that of CN, well enough?

5.1. Excitation conditions

CN is not the only photo-dissociation sensitive molecule displaying surprising low excitation temperatures. From a spatially resolved, two-transition study, Henning et al. (2010) find that C_2H display the very same behavior, which cannot be represented with current chemical models. While the debate remains possible for CN, the chemistry of C_2H is relatively well known, so the coincidence points towards a general problem to retain molecules at low temperatures in protoplanetary disks.

In all chemical models, HCN is formed closer to the midplane than CN, at densities high enough to thermalize the HCN $J = 1$–0 transition (5×10^5 cm^{-3}, Guilloteau & Baudry 1981; Monteiro & Stutzki 1986). The HCN excitation temperature

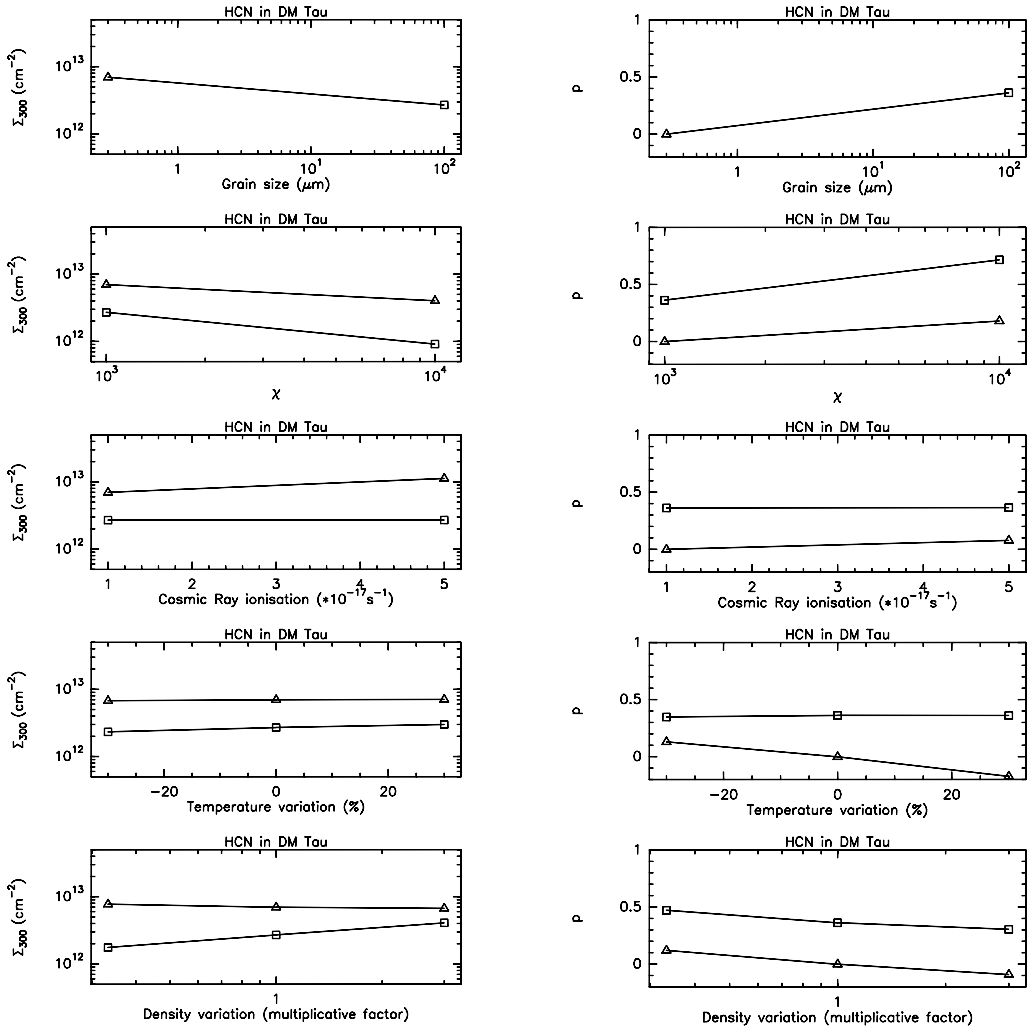

Fig. 7. Variations in the radial distribution of HCN (Σ_{300} and p parameters) according to the maximum grain size a_+, the UV field intensity (χ factor), the rate of cosmic ray ionization, and modification of the physical structure. The "standard" values are $\chi = 10^3$, CR $= 10^{-17}$ s^{-1}, and nominal temperature and density structure. Squares: big grains ($a_+ = 0.1$ mm); triangles: small grains ($a_+ = 0.3\,\mu$m).

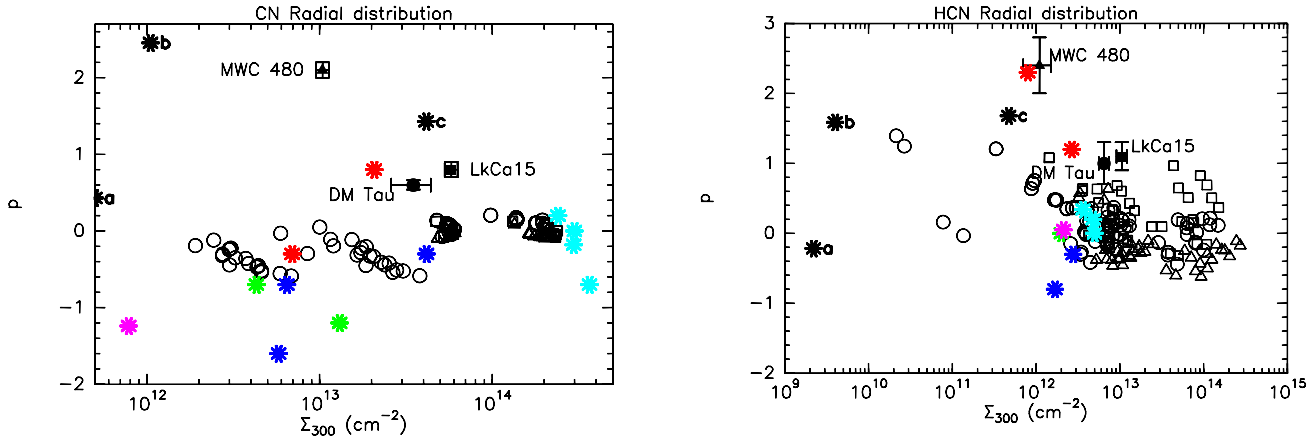

Fig. 8. Value of Σ_{300} and p for the three sources DM Tau (circle), LkCa 15 (square), and MWC 480 (triangle). Our observations are plotted in filled black markers, the results from the PDR chemical modeling are in open markers. In the DM Tau case, we also plot the results with the photodissociation rates calculated for a black body at 4000 K from van Dishoeck et al. (2006). Results from the literature are marked with stars; red: Aikawa & Herbst (1999); green: Aikawa et al. (2002); blue: van Zadelhoff et al. (2003); cyan: Aikawa & Nomura (2006); magenta: Willacy & Langer (2000); and black: Willacy et al. (2006) (a, b and c correspond to their $K = 0, K = 10^{16}$ and $K = 10^{18}$ cases). The error bars show the power-law fitting errors (1σ).

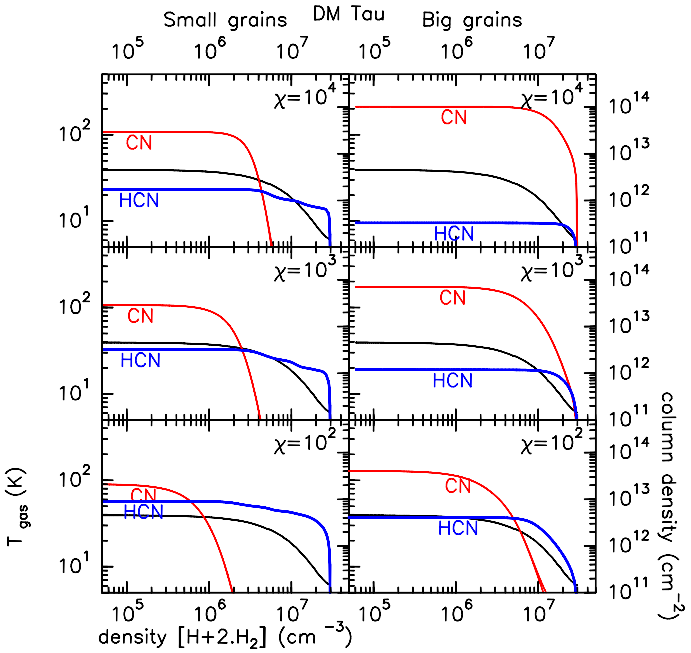

Fig. 9. Cumulative CN (red) and HCN (blue) column densities and temperature (black) from the midplane to the atmosphere as a function of the density at a radius of 304 AU in the DM Tau disk. Models with temperature fixed from the structure file. This samples only half of the disk, so the column densities have to be multiplied by 2 to retrieve the Σ values.

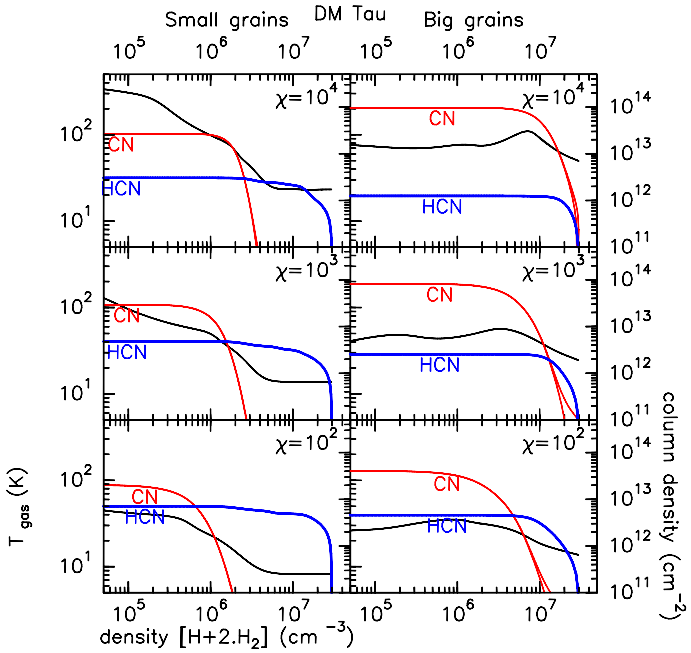

Fig. 10. Same as Fig. 9 for models with thermal balance computed.

derived from our observations is then expected to reflect the kinetic temperature of the disk midplane in the region where the J = 1–0 line is optically thick, that is up to about 150 AU in DM Tau and LkCa 15. The values derived from the observations are ≃6 K for DM Tau and ≃12 K for LkCa 15, the excitation temperature for MWC 480 remaining unconstrained. On the other hand, CN is expected to be mainly formed (at least largely formed) in the upper layer, close to the disk surface. Although the overall finding that T(CN) > T(HCN) in both sources is in qualitative agreement with this expectation, the observed values are surprisingly low.

From Fig. 9, for all models with small grains, 80% of the CN column density builds up in a region where the kinetic temperature is ≥30 K. Furthermore, 50% of this column density originates in regions where the density is at least $5-8\times10^5$ cm^{-3}, and CN is not present at all for densities exceeding about 3×10^6 cm^{-3}, i.e. below two scale heights. This contradicts the observations that indicate that the bulk of CN is near the disk plane ($\alpha_d < 1$ at the 3σ level).

While all published disk chemical models clearly have high CN abundances only at large heights, deriving the densities and temperatures at which the bulk of the CN column density is built is often not possible, as most studies have focused more on the general behavior of the chemistry than on detailed line emission predictions. Nevertheless, we note that Walsh et al. (2010) only have a substantial amount of CN for $T > 20$ K and $n > 10^6$ cm^{-2}, at rather large z/r, as in our model.

The comparison with other transitions, CN(1–0) and CN(3–2) show that for MWC 480, our model predicts a stronger CN(3–2) line (9.0 Jy km s^{-1}) than observed. This can be ascribed to partial subthermal excitation for this transition, as its critical density is $3-6 \times 10^6$ cm^{-3}. For DM Tau, our predictions for the CN J = 1–0 agree with the observations of Dutrey et al. (1997), but there is no published data on the CN(3–2) line. For the disk of LkCa15, our best-fit model underestimates the line flux of the CN(3–2) line by 30%. Raising the rotation temperature to about 25 K brings the predicted line flux in better agreement for this transition. This suggests that a fraction of the CN molecules lie in a warmer (and dense enough) temperature region. However, although the exact collision rates for CN with H_2 are unknown, the densities are high enough to be close to thermalization for the observed lines, and it is likely that $T_{rot} > T_k/2$, so explaining temperatures below 15 K by significant subthermal excitation appears difficult.

5.2. Surface densities of CN and HCN

A general prediction of all chemical models is that the surface densities of CN and HCN are nearly constant as a function of radius $p \simeq 0$. The observed slopes are larger, ≃1, and the separate hyperfine CN analysis even suggests a steepening of the surface density distribution at larger radii. Furthermore, changing the model disk mass to one third or three times the nominal value only changes the surface density of CN and HCN by about 10–20% (see Figs. 6, 7 and B.1).

Bergin et al. (2003) show that Ly α radiation significantly affects the relative photodissociation rates of HCN and CN. In our model, the impact of the Ly α line on CN is quite low. This is because the direct production of CN from the photodissociation of HCN (HCN + $h\nu$ → CN + H) is not in general the main production path of CN. Figure 12 presents the main chemical reaction leading to the formation of CN at a radius of 304 AU. Photodissociation of HCN is the most efficient CN production mechanism only in a small region with high HCN abundance. Upwards in the disk, the main CN formation reactions are N + CH → CN + H and N + C_2 → CN + C, so that the overall abundance of CN is controlled by the abundance of atomic nitrogen. However, HCN decreases with Lyα intensity, so that the CN/HCN ratio depends on the Lyα flux (as also found by Fogel et al. 2011). We find, however, that the effect is very small when dust is composed of small dust grains. With large grains, the HCN column density is divided by a factor ≃2.5 for a Ly α line

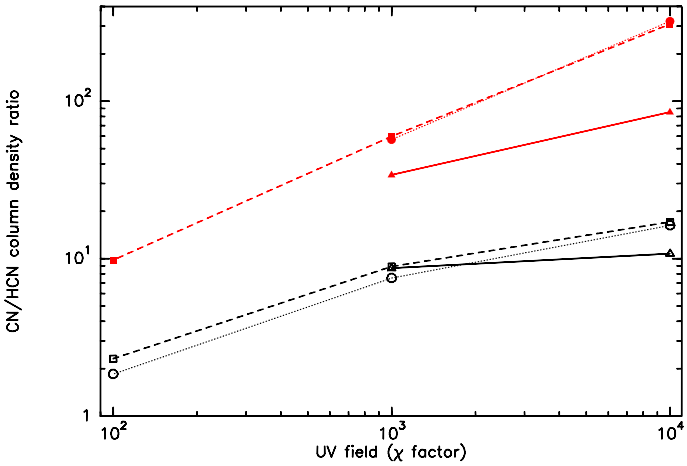

Fig. 11. CN/HCN column density ratios as a function of the UV field at R = 97 AU (triangles), 304 AU (squares), and 602 AU (circles) for the models with small grains (thick black lines) and big grains (thin red lines).

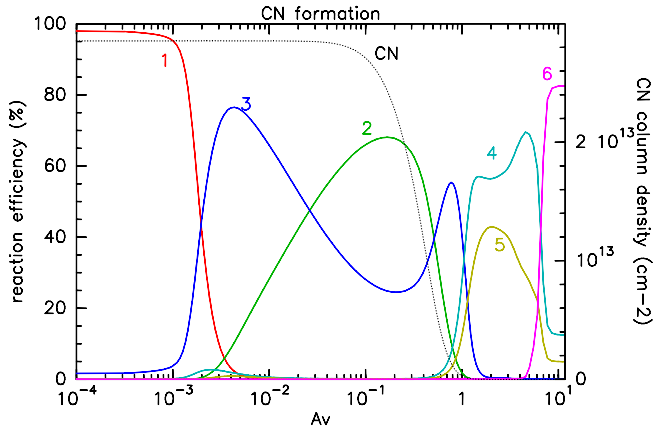

Fig. 12. Efficiency of CN formation reactions at R = 304 AU for DM Tau with small grains, $\chi = 10^3$, CR = 10^{-17} s^{-1}. Only the main reactions are plotted (i.e. more than 10%): 1 (red): H + CN^+ → H^+ + CN; 2 (green): N + C_2 → CN + C; 3 (blue): N + CH → CN + H; 4 (cyan): HCN + photon → CN + H; 5 (yellow): HNC + photon → CN + H; 6 (magenta): OCN + photon → O + CN. The cumulative CN column density is plotted in black.

contributing to one third of the UV luminosity. This is consistent with the Fogel et al. (2011) results where the effect is of Ly α is only visible for settled grain models (i.e. models with a reduced UV extinction in the upper layers, as for large grains).

Finally, PDR models also predict that the CN/HCN ratio increases with grain size because large grains allow UV flux to penetrate deeper in the disk. This effect is illustrated in Fig. 11. The high CN/HCN ratio (4 to 10 at 300 AU) in the three sources agree with the presence of large grains in the three disks. On the other hand, the Aikawa & Nomura (2006) results suggest a rather weak dependency of the CN/HCN ratio on the grain sizes. However, this study explored much bigger grain sizes than we do here, but the differences between their 10 μm and 1 mm case are similar to our findings. Walsh et al. (2010) also find that the CN/HCN ratio increases when surface chemistry is included, as nitrogen can be incorporated into larger molecules in the disk's midplane.

5.3. Toward a cold molecular layer?

We investigate here mechanisms that would partially provide cold molecular material close to the midplane.

5.3.1. Large grains

Grain growth can bring molecules closer to the disk midplane, by allowing UV radiation to penetrate deeper in the disk structure. Figure 9 also indicates that the only case in which CN is produced in sufficient quantities at low temperatures is the high UV ($\chi = 10^4$), big grains $a_+ = 0.1$ mm case, where 50% of the CN column density builds up at temperatures below 10 K, and the rest between 10 and 20 K. However, neglecting freeze-out and surface chemistry in this case is unlikely to be valid. Moreover, in this case, the disk temperature and density structure were imposed a priori, and are not consistent with the impinging UV field and its attenuation. If we compute the thermal balance assuming the incident UV field is the only heating source, while keeping the same density structure, the picture changes completely (Fig. 10). The whole gaseous disk becomes warm, the minimum temperature being 60 K. Furthermore, 90% of the CN column density is built up at densities above 10^6 cm^{-3}, thus subthermal excitation also becomes unlikely.

Enhanced photodesorption would bring larger amounts of (cold) CN, HCN, and C_2H near the disk's midplane. Willacy & Langer (2000) checked this possibility using moderate grain growth, but it does not provide enough cold gas. Doing the same calculation within larger grains appears, however, as an interesting clue to partially reconcile observations and models.

5.3.2. Turbulent mixing

Turbulent transport could bring CN and C_2H formed in the warm upper layers down to the disk midplane, where they would cool very quickly. The main difficulty is to avoid sticking onto cold dust grains. Hersant et al. (2009) explored this for CO molecules, and found that turbulent diffusion does not affect the total amount of CO much, but could bring a small fraction of it to low temperatures. Willacy et al. (2006) managed to get a substantial amount of CN towards the disk plane, but only using a large diffusion coefficient, 10^{-18} cm^2 s^{-1}, which is ten times more than expected from our current estimates of the viscosity (α viscosity parameter below 0.01) in disks. We note, however, that the model predictions are (at least for CN) not too far from the observed column densities. The low mixing efficiency, which is a result of dilution (the gas density in the upper layer being much lower than in the disk midplane, see also Semenov et al. 2006) may thus not be a major problem, as we only want to bring the existing CN molecules to low temperature regions, but not to significantly increase the total amount of CN.

5.3.3. Lowering the gas-to-dust ratio

In our resolved observations, Σ_d is actually geometrically constrained by measuring the height above the disk midplane where the molecules are located; it is expressed as a column density by simply scaling to the total disk surface density (see Eq. (6)). When assuming $\kappa_\nu(230\,\mathrm{GHz}) = 2$ cm^2 g^{-1} (of dust) and a canonical gas-to-dust ratio of 100, the measured "depletion" column density, Σ_d, appears ~4–10 times higher than predicted from chemical models (see in particular Aikawa & Nomura 2006). Aikawa & Nomura (2006) also show that Σ_d does not strongly depend on the grain size: so what controls the location of the CN layer (and those of other molecules) is essentially the column

density of hydrogen towards the disk surface. Lowering the gas-to-dust ratio to 20 (or reducing the hydrogen surface density by a factor 5), we bring to first order the observed Σ_d in rough agreement with the model prediction. In such a case, CN would be present in regions where the density is low enough (a few 10^5 cm^{-3}) to lead to substantial subthermal excitation.

We checked this possibility by using our PDR and radiative transfer codes in a disk six times less massive than our nominal assumption. The excitation is computed using the modified LVG approximation described in Pavlyuchenkov et al. (2007), who also show that this is a reasonably accurate solution for the radiative transfer in disks. The collision rates for CN were assumed to be identical to those of HCN with He (Green & Thaddeus 1974). For DM Tau, using the tapered edge surface density profile, we indeed find $\Sigma_d = 1.7 \pm 0.1 \times 10^{21}$ cm^{-2}, and a kinetic temperature of 15–20 K. Given the uncertainties on the collision rates, such a solution appears compatible with the expected temperature range in the molecular rich region. Such a low gas-to-dust ratio would also provide an appropriate explanation for the low temperatures also derived from C_2H by Henning et al. (2010).

Unfortunately, with our chemical model, such low disk masses result in predicted HCN and CN column densities that are substantially lower than observed, so that this mechanism is not fully satisfactory to explain the observations. Imaging higher lying transitions, which have higher critical densities than the $J = 2$–1 line observed here, could give more accurate constraints.

Rather than changing the gas-to-dust ratio, raising the mm wave dust absorption coefficient by a similar factor is also a strictly equivalent alternative, and leads to the same low disk masses (0.003 $M_\odot$ for DM Tau). However, our assumed value of $\kappa(1.3\ \mathrm{mm}) = 2\ \mathrm{cm}^2\ \mathrm{g}^{-1}$ (of dust) already appears high (see e.g. Draine 2006, and references therein).

5.3.4. Low temperature chemistry

Finally, Hily-Blant et al. (2008) have observed very cold ^{13}CN in the nuclei of a few dense cores of known temperature and density ($T \sim 6$–10 K, $n \sim 10^4$–10^6 cm^{-3}), which present temperature and densities that are relatively similar to those encountered in the midplanes of T Tauri disks. They find that CN is not strongly depleted in the nuclei of the cores, in contrast to CO, and can be a fair column density tracer in these extreme conditions. However, Hily-Blant et al. (2010) were unable to account for the near constancy of the CN/HCN ratio in their chemical models. These observations also leave open the possibility that cold chemistry is not fully understood at least for CN. Hily-Blant et al. (2010) conclude that our knowledge of the low temperature chemistry of CN is limited by the extrapolation of the rate coefficients measured at high temperatures to the 10 K regime for many of the important reactions, including those mentioned in Sect. 5.2 (Pineau des Forets et al. 1990; Boger & Sternberg 2005). However, at such low temperatures and high densities, chemistry also depends on reactions on the grain surfaces, as shown by Walsh et al. (2010), in particular for HCN. Therefore, another viable alternative would be inadequate knowledge of the grain surface chemistry.

6. Summary

We present sensitive, high spatial and spectral resolution observations of HCN $J = 1$–0 and CN $J = 2$–1 in 2 T Tauri disks (DM Tau and LkCa 15) and one Herbig Ae (MWC 480). Column densities and excitation conditions are recovered through a minimization scheme that utilizes all the information provided by the hyperfine structure of the observed transitions. Although we find out $T(\mathrm{CN}) > T(\mathrm{HCN})$ as expected from a layered disk structure, the analysis indicates that the location of CN and its apparent excitation temperature appear incompatible with the expectations from current chemical models. Lowering the gas-to-dust ratio might partially solve the conflict on temperature and localization of the molecules, but may not produce large enough quantities of CN and HCN. The observations thus suggest that a substantial fraction of the molecules are created in the disk plane at low temperatures, perhaps by surface chemistry. Sensitive, spatially resolved images of higher excitation lines of CN and HCN would be required to provide a complete diagnostic to determine the excitation conditions in disks, allowing us to decide between the possible options.

Acknowledgements. We acknowledge all the Plateau de Bure IRAM staff for their help during the observations. We thank Pierre Hily-Blant for his modifications of a previous version of the PDR code. We also acknowledge Franck Le Petit for many fruitful discussions about the PDR code. This research was supported by the program PCMI from INSU/CNRS.

References

Aikawa, Y. 2007, ApJ, 656, L93
Aikawa, Y., & Herbst, E. 1999, A&A, 351, 233
Aikawa, Y., & Nomura, H. 2006, ApJ, 642, 1152
Aikawa, Y., van Zadelhoff, G. J., van Dishoeck, E. F., & Herbst, E. 2002, A&A, 386, 622
Aikawa, Y., Momose, M., Thi, W.-F., et al. 2003, PASJ, 55, 11
Bergin, E., Calvet, N., D'Alessio, P., & Herczeg, G. J. 2003, ApJ, 591, L159
Bergin, E. A., Aikawa, Y., Blake, G. A., & van Dishoeck, E. F. 2007, in Protostars and Planets V, ed. B. Reipurth, D. Jewitt, & K. Keil, 751
Boger, G. I., & Sternberg, A. 2005, ApJ, 632, 302
Burke, J. R., & Hollenbach, D. J. 1983, ApJ, 265, 223
Burton, M. G., Hollenbach, D. J., & Tielens, A. G. G. M. 1990, ApJ, 365, 620
Chapillon, E., Guilloteau, S., Dutrey, A., & Piétu, V. 2008, A&A, 488, 565
Chiang, E. I., & Goldreich, P. 1997, ApJ, 490, 368
D'Alessio, P., Calvet, N., Hartmann, L., Lizano, S., & Cantó, J. 1999, ApJ, 527, 893
D'Alessio, P., Calvet, N., Hartmann, L., Franco-Hernández, R., & Servín, H. 2006, ApJ, 638, 314
Dartois, E., Dutrey, A., & Guilloteau, S. 2003, A&A, 399, 773
Draine, B. T. 2006, ApJ, 636, 1114
Dutrey, A., Guilloteau, S., & Guelin, M. 1997, A&A, 317, L55
Dutrey, A., Henning, T., Guilloteau, S., et al. 2007, A&A, 464, 615
Fogel, J. K. J., Bethell, T. J., Bergin, E. A., Calvet, N., & Semenov, D. 2011, ApJ, 726, 29
Goicoechea, J. R., Pety, J., Gerin, M., et al. 2006, A&A, 456, 565
Green, S., & Thaddeus, P. 1974, ApJ, 191, 653
Guilloteau, S., & Baudry, A. 1981, A&A, 97, 213
Guilloteau, S., & Dutrey, A. 1998, A&A, 339, 467
Guilloteau, S., Dutrey, A., Piétu, V., & Boehler, Y. 2011, A&A, 529, A105
Henning, T., Semenov, D., Guilloteau, S., et al. 2010, ApJ, 714, 1511
Herbig, G. H., & Goodrich, R. W. 1986, ApJ, 309, 294
Hersant, F., Wakelam, V., Dutrey, A., Guilloteau, S., & Herbst, E. 2009, A&A, 493, L49
Hily-Blant, P., Walmsley, M., Pineau Des Forêts, G., & Flower, D. 2008, A&A, 480, L5
Hily-Blant, P., Walmsley, M., Pineau Des Forêts, G., & Flower, D. 2010, A&A, 513, A41
Kastner, J. H., Zuckerman, B., Weintraub, D. A., & Forveille, T. 1997, Science, 277, 67
Kastner, J. H., Zuckerman, B., Hily-Blant, P., & Forveille, T. 2008, A&A, 492, 469
Le Bourlot, J., Pineau Des Forets, G., Roueff, E., & Flower, D. R. 1993, A&A, 267, 233
Le Petit, F., Nehmé, C., Le Bourlot, J., & Roueff, E. 2006, ApJS, 164, 506
Mannings, V., Koerner, D. W., & Sargent, A. I. 1997, Nature, 388, 555
Monteiro, T. S., & Stutzki, J. 1986, MNRAS, 221, 33P
Öberg, K. I., Qi, C., Fogel, J. K. J., et al. 2010, ApJ, 720, 480
Pavlyuchenkov, Y., Semenov, D., Henning, T., et al. 2007, ApJ, 669, 1262

Pety, J. 2005, in SF2A-2005: Semaine de l'Astrophysique Française, ed. F. Casoli, T. Contini, J. M. Hameury, & L. Pagani, 721
Piétu, V., Dutrey, A., Guilloteau, S., Chapillon, E., & Pety, J. 2006, A&A, 460, L43
Piétu, V., Dutrey, A., & Guilloteau, S. 2007, A&A, 467, 163
Pineau des Forets, G., Roueff, E., & Flower, D. R. 1990, MNRAS, 244, 668
Qi, C., Ho, P. T. P., Wilner, D. J., et al. 2004, ApJ, 616, L11
Qi, C., Wilner, D. J., Aikawa, Y., Blake, G. A., & Hogerheijde, M. R. 2008, ApJ, 681, 1396
Schreyer, K., Guilloteau, S., Semenov, D., et al. 2008, A&A, 491, 821
Semenov, D., Wiebe, D., & Henning, T. 2006, ApJ, 647, L57
Semenov, D., Pavlyuchenkov, Y., Henning, T., Wolf, S., & Launhardt, R. 2008, ApJ, 673, L195
Simon, M., Dutrey, A., & Guilloteau, S. 2000, ApJ, 545, 1034
Thi, W.-F., van Zadelhoff, G.-J., & van Dishoeck, E. F. 2004, A&A, 425, 955
van Dishoeck, E. F., Jonkheid, B., & van Hemert, M. C. 2006, Faraday Discuss., 133, 231
van Zadelhoff, G.-J., van Dishoeck, E. F., Thi, W.-F., & Blake, G. A. 2001, A&A, 377, 566
van Zadelhoff, G.-J., Aikawa, Y., Hogerheijde, M. R., & van Dishoeck, E. F. 2003, A&A, 397, 789
Walsh, C., Millar, T. J., & Nomura, H. 2010, ApJ, 722, 1607
Westley, M. S., Baragiola, R. A., Johnson, R. E., & Baratta, G. A. 1995, Nature, 373, 405
Willacy, K., & Langer, W. D. 2000, ApJ, 544, 903
Willacy, K., Langer, W., Allen, M., & Bryden, G. 2006, ApJ, 644, 1202

Pages 15 to 22 are available in the electronic edition of the journal at http://www.aanda.org

Appendix A: Channel maps

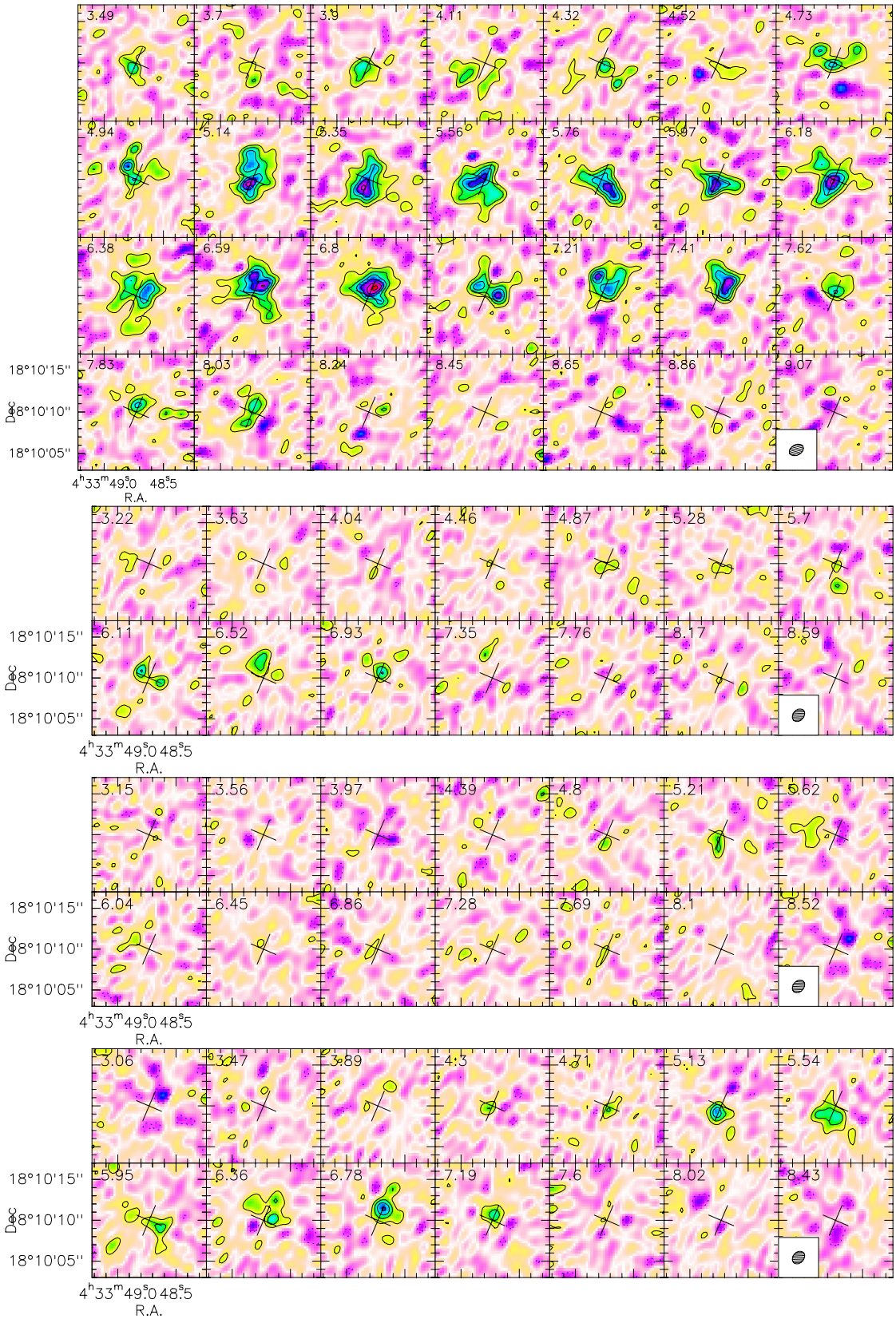

Fig. A.1. Channel maps of CN hyperfine components towards DM Tau. *From top to bottom*, the velocity scales are referred to 226.874745 GHz (3 blended components), 226.679382 GHz, 226.663703 GHz, and 226.659575 GHz. Note the better spectral resolution in the top panel. The spatial resolution is $1.7 \times 1.2''$ at PA 120°, contour spacing is 53 mJy/beam, or 0.61 K, corresponding to 2.0σ in the upper panel, and 2.3σ in the lower ones.

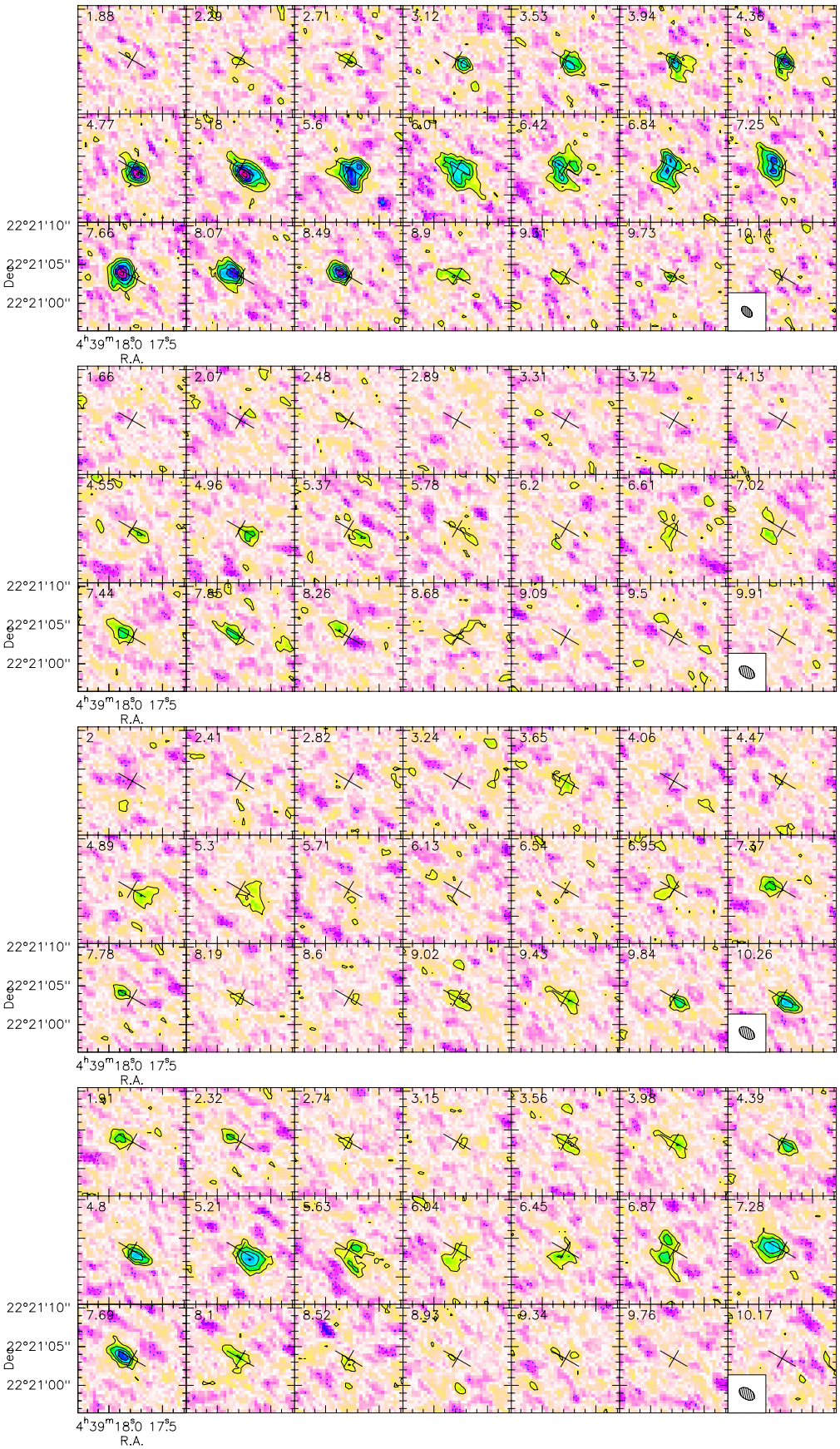

Fig. A.2. As Fig. A.1, but towards LkCa15. All panels use the same spectral resolution. Note the repeated channels in the two bottom panels, as the velocity spacing between these components is 5 km s^{-1}, i.e. 12 channels. The spatial resolution is $1.7 \times 1.0''$ at PA 44°, contour spacing is 60 mJy/beam, or 0.81 K and 2.1σ.

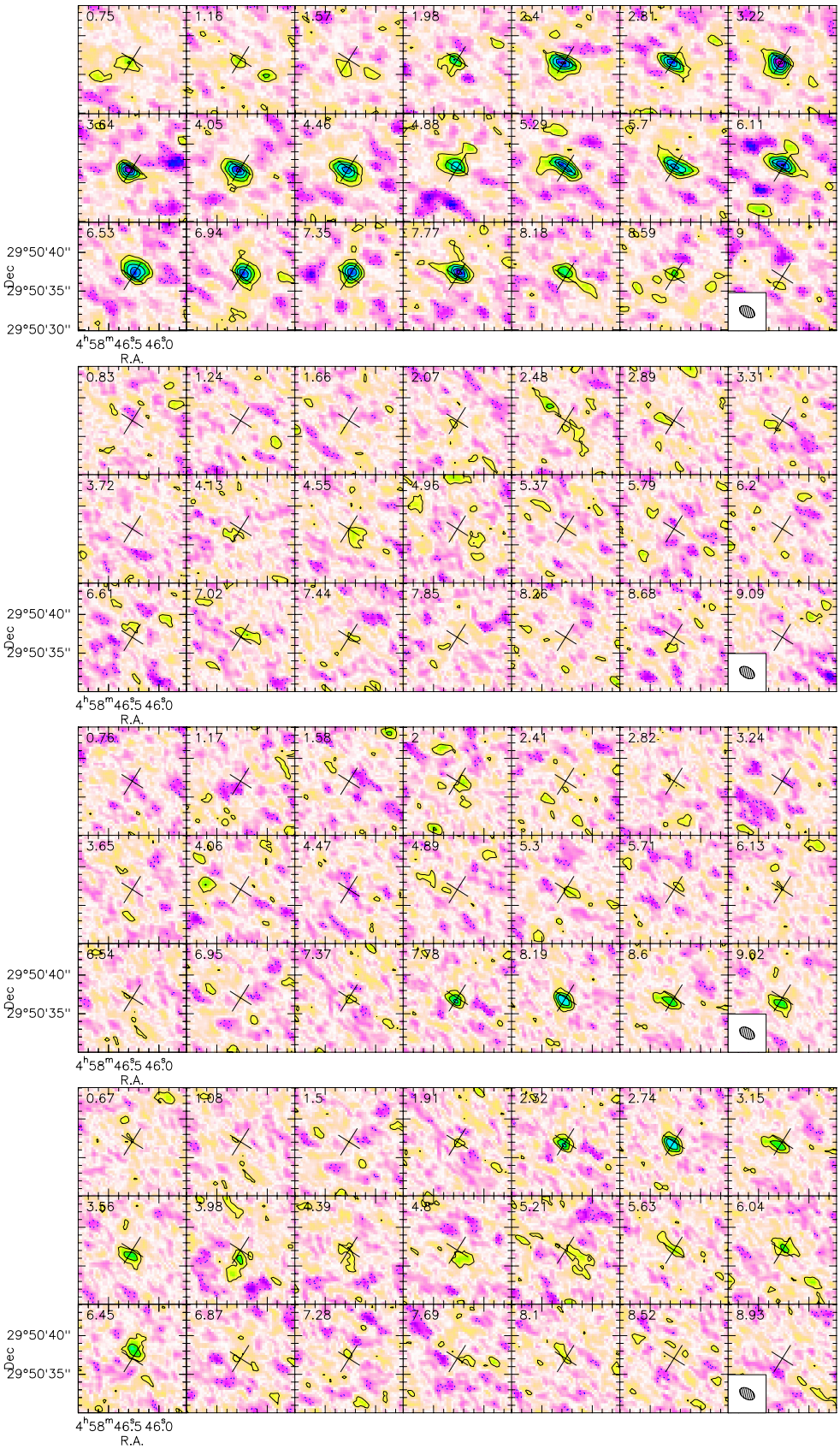

Fig. A.3. As Fig. A.2, but towards MWC 480. The spatial resolution is $2.2 \times 1.35''$ at PA 60°, contour spacing is 55 mJy/beam, or 0.45 K and 2σ. The high rotation velocity result in an overlap of emission between the two hyperfine components in *the bottom panels*.

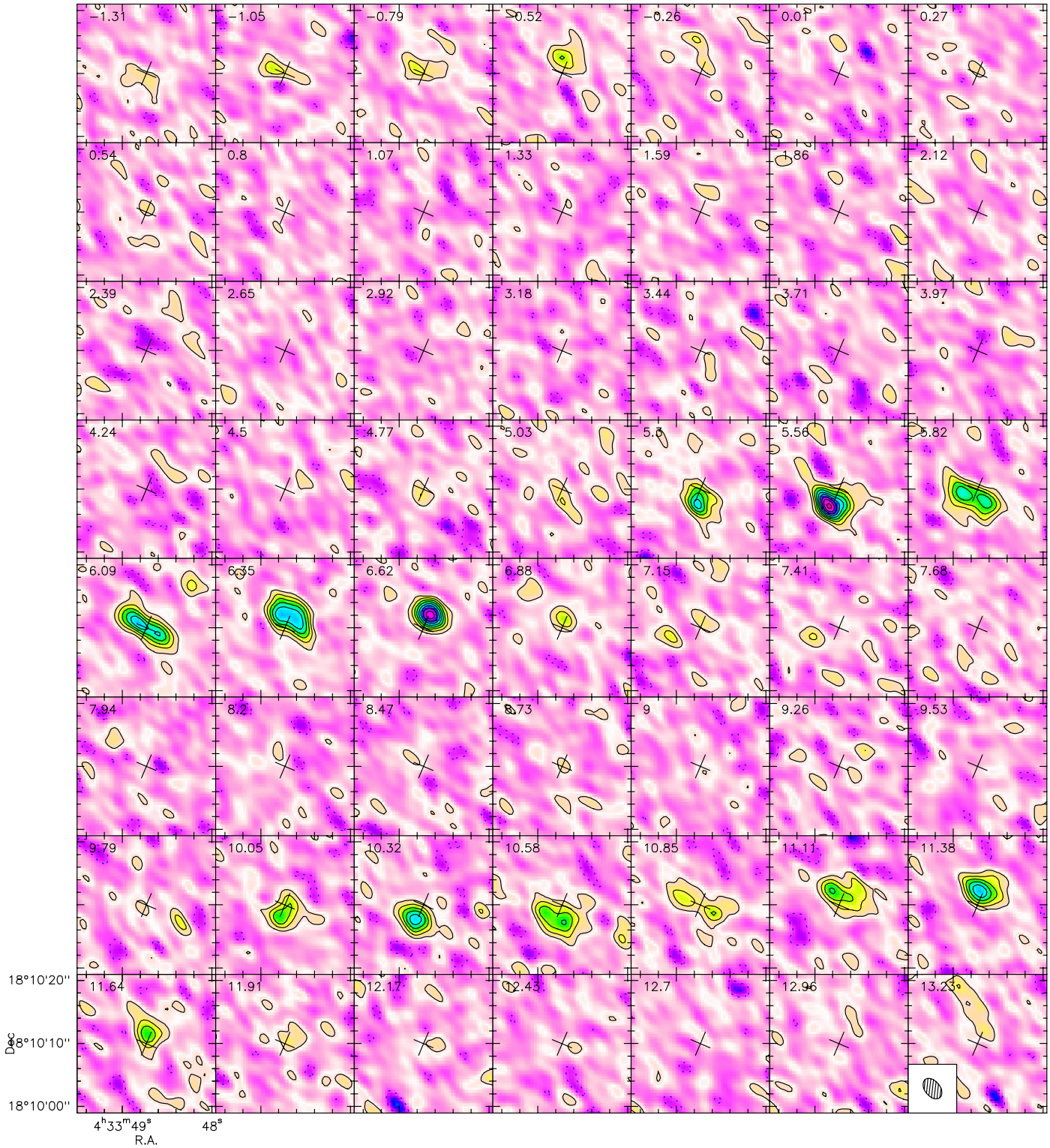

Fig. A.4. Channel maps of HCN hyperfine components towards DM Tau. The spatial resolution is 3.7 × 2.4″ at PA 39°, and contour spacing is 12 mJy/beam, or 0.21 K, 2.0σ.

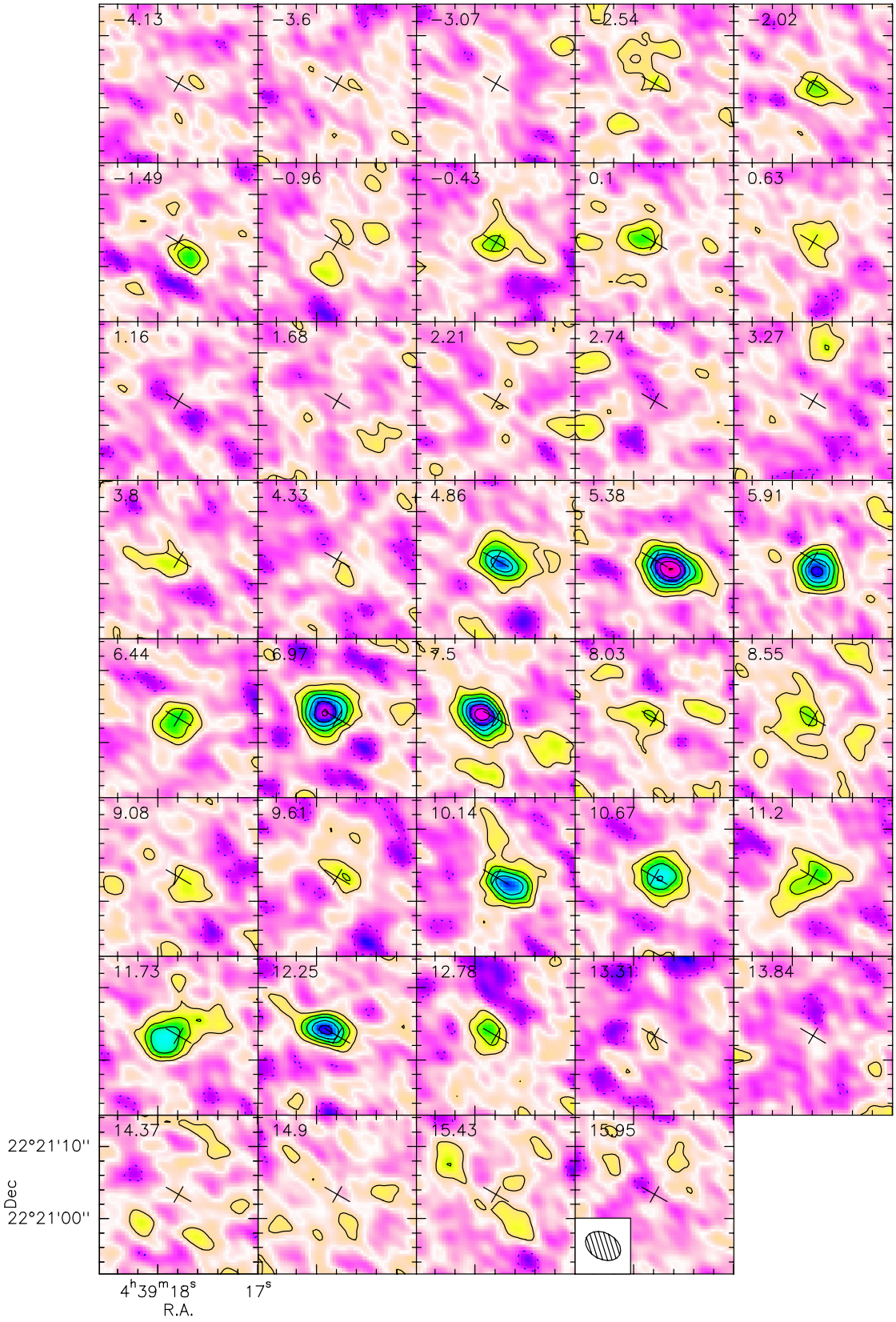

Fig. A.5. Channel maps of HCN hyperfine components towards LkCa15. The spatial resolution is 4.1 × 2.9″ at PA 51°, contour spacing is 16 mJy/beam, or 0.21 K and 2.0σ.

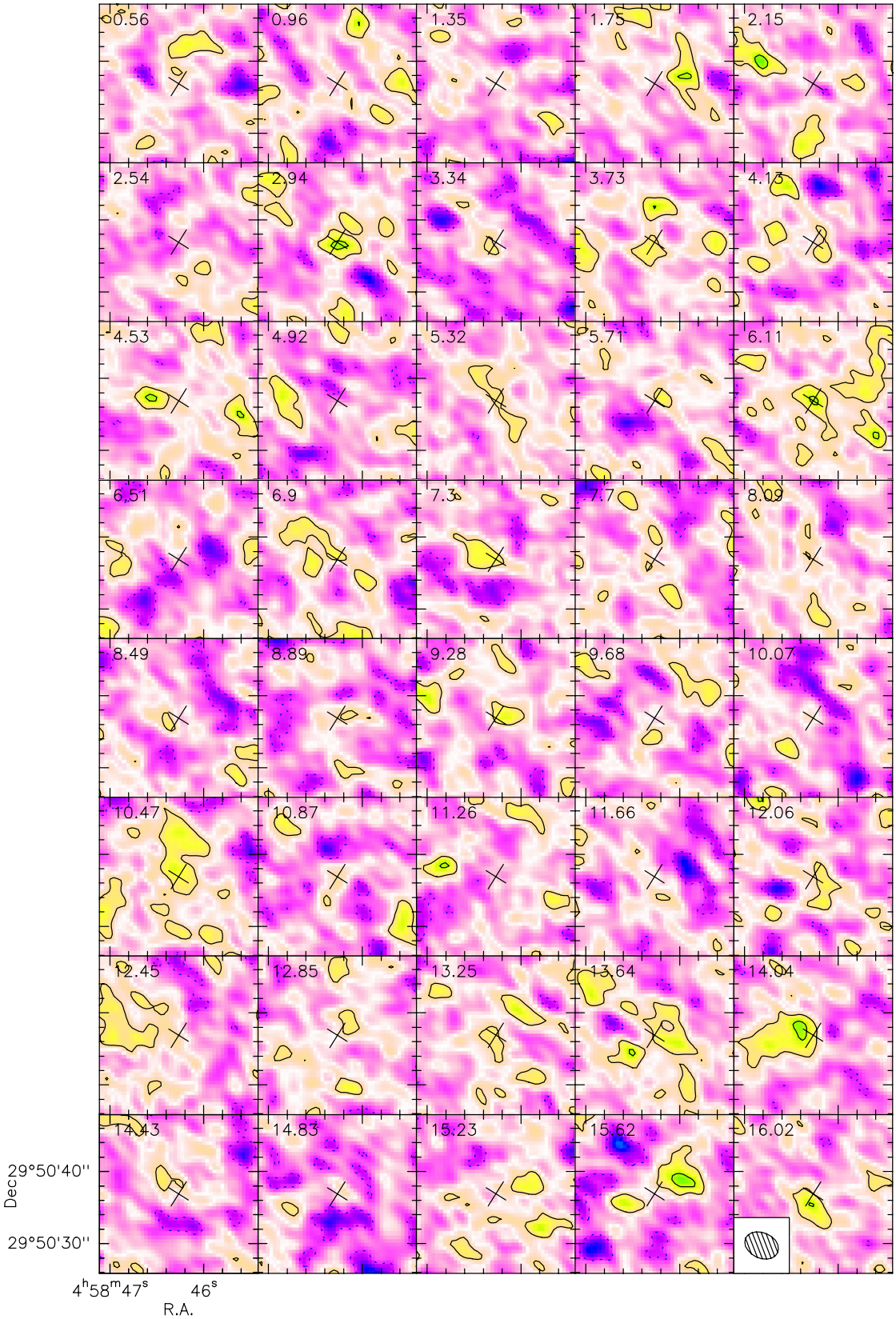

Fig. A.6. Channel maps of HCN hyperfine components towards MWC 480. The spatial resolution is 4.5 × 3.6″ at PA 66°, contour spacing is 16 mJy/beam, or 0.15 K and 1.8σ.

Appendix B: Chemical model results

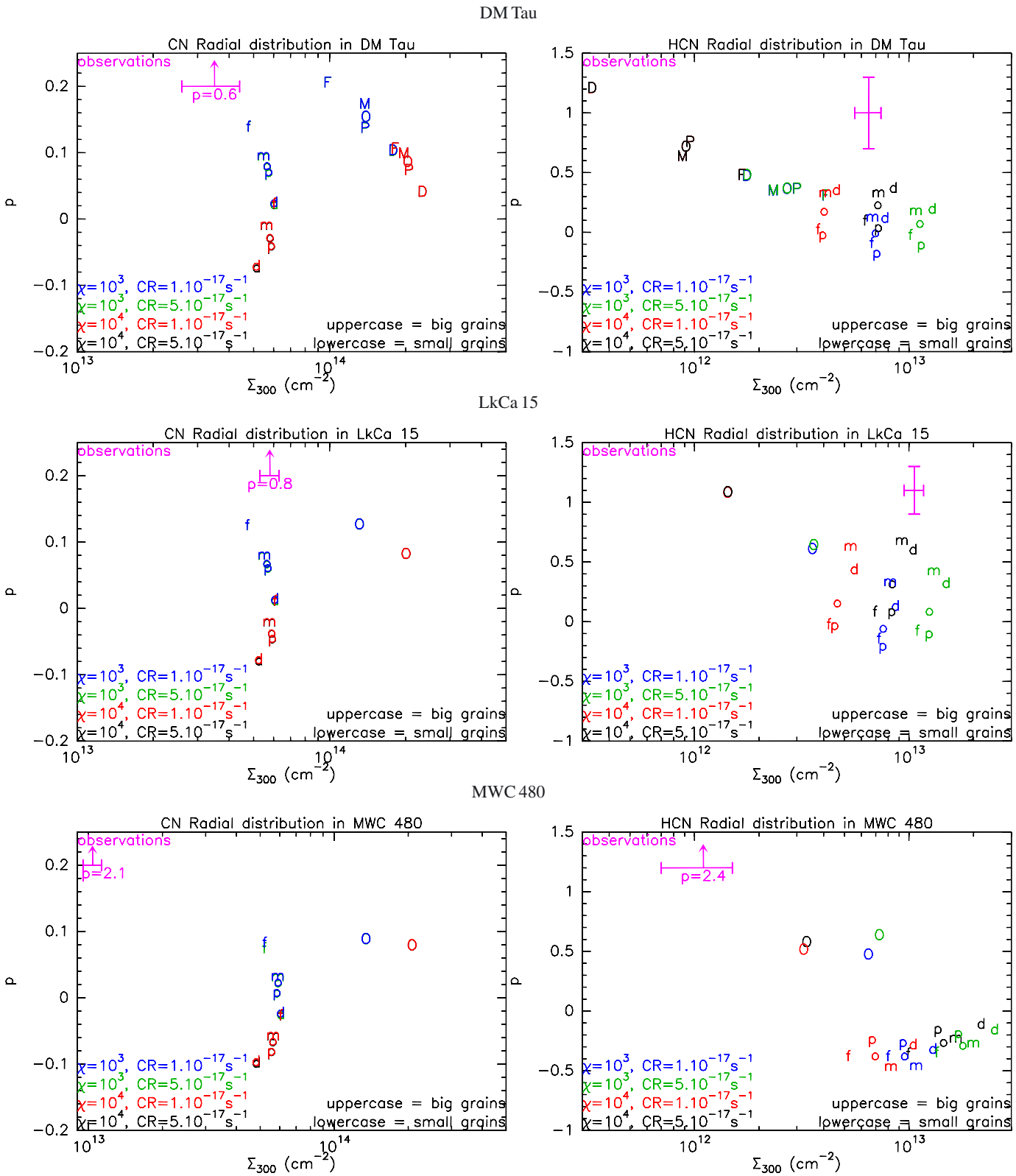

Fig. B.1. Value of Σ_{300} and p from our chemistry modeling for the three sources, with our "standard" chemistry. o: density and temperature from theoretical models, p: temperature increased by 30%, m: temperature decreased by 30%, f: density multiplied by a factor 3 and d: density divided by a factor 3. In many models the blue and green markers overlap, as do the red and black ones.

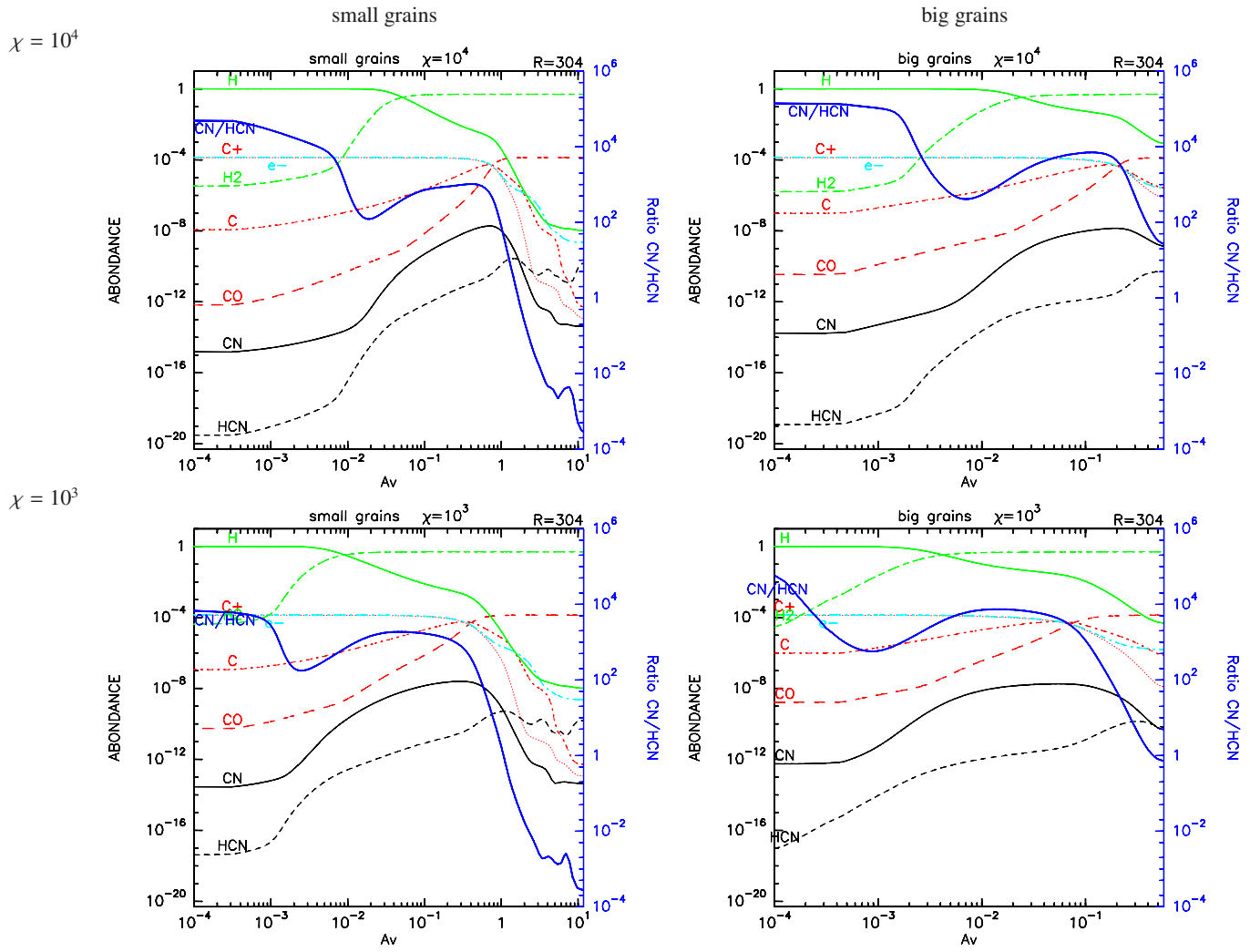

Fig. B.2. H, H_2, C^+, C, CO, CN, HCN abundance and CN/HCN ratio as a function of opacity from atmosphere ($A_v = 0$) to midplane at $R = 304$ AU for DM Tau with CR = 10^{-17} s^{-1}.